The Meteoritical Society

Meteoritics & Planetary Science 1–23 (2016)
doi: 10.1111/maps.12659

Igneous cooling history of olivine-phyric shergottite Yamato 980459 constrained by dynamic crystallization experiments

Emily FIRST* and Julia HAMMER

Department of Geology & Geophysics, University of Hawai'i at Mānoa, 1680 East-West Road, POST 606A, Honolulu, Hawai'i 96822, USA
*Corresponding author. E-mail: efirst@hawaii.edu

(Received 26 July 2015; revision accepted 29 March 2016)

Abstract–Dynamic crystallization experiments were performed on a liquid having the bulk composition of olivine-phyric shergottite Yamato 980459, to constrain the igneous thermal history of this meteorite. Key characteristics of the meteorite's mineralogy and texture, including several morphologically distinct olivine and pyroxene crystal populations and a glassy mesostasis devoid of plagioclase, were replicated upon cooling from 1435 to 909 °C at 1 atmosphere under reducing conditions. Three sequential cooling ramps are required to produce synthetic samples with textures and compositions matching Yamato 980459. Olivine phenocrysts formed at <1 °C h^{-1}, presumably at depth in the Martian crust. Pyroxene phenocrysts formed mainly at ~10 °C h^{-1}, consistent with crystallization within a lava flow at depths of 25–45 cm. Increased cooling rate (~100 °C h^{-1}) in a third stage suppressed the formation of plagioclase and produced groundmass crystals, consistent with crystallization at lava flow depths of 5–7 cm. Although Y 980459 is unique among Martian meteorites (i.e., preserving a primary glassy mesostasis), its emplacement did not require unique physical conditions. Rather, the second and third cooling stages may reflect cooling within the core of a pāhoehoe-like flow and subsequent breakout on the surface of Mars.

INTRODUCTION

The thermal history of a volcanic rock is closely linked with its emplacement mechanism on a planet's surface. For example, explosively erupted pyroclasts cool through the solidus about a million times faster than do lava lake interiors (Wright and Okamura 1977; Lloyd et al. 2013). Thus, constraining the igneous cooling rates of Martian meteorites is important to the interpretation of volcanic processes on Mars. Cooling rates of igneous rocks are estimated by a variety of means, both qualitative and quantitative, the most robust of which rely on experimentally calibrated data linking petrographic observables with known thermal history. Extant approaches are based on crystal morphology alone (e.g., Faure et al. 2003, 2007), crystal composition (e.g., Mollo et al. 2010), crystal composition and qualitative sample and crystal texture (e.g., McCoy and Lofgren 1999), quantitative crystal texture (e.g., Lentz and McSween 2005; Hammer 2009), and chemical diffusion rates (e.g., Miyamoto et al. 1986, 2009b). Estimations of cooling rate by comparison to experimental results from studies on unrelated materials are also common (e.g., McCoy et al. [1992] referencing Walker et al. 1978; Treiman and Sutton [1992] referencing Lofgren et al. 1974). Uncertainties are amplified when relevant experimental datasets (e.g., using similar whole-rock compositions) are not available. Thus, experimental studies on specific compositions are necessary to accurately interpret igneous cooling rates.

The olivine-phyric shergottite Yamato 980459 (Y-980459; Fig. 1) is proposed to have erupted as a thin lava flow (e.g., Greshake et al. 2004; Usui et al. 2008), based on the high cooling rates implied by its vitrophyric matrix. The range is quantified by Greshake et al. (2004) at 1450–1890 °C h^{-1} using textural comparisons with experimental studies on various bulk compositions (Donaldson 1976; Faure et al. 2003). Other studies consider crystal populations separately,

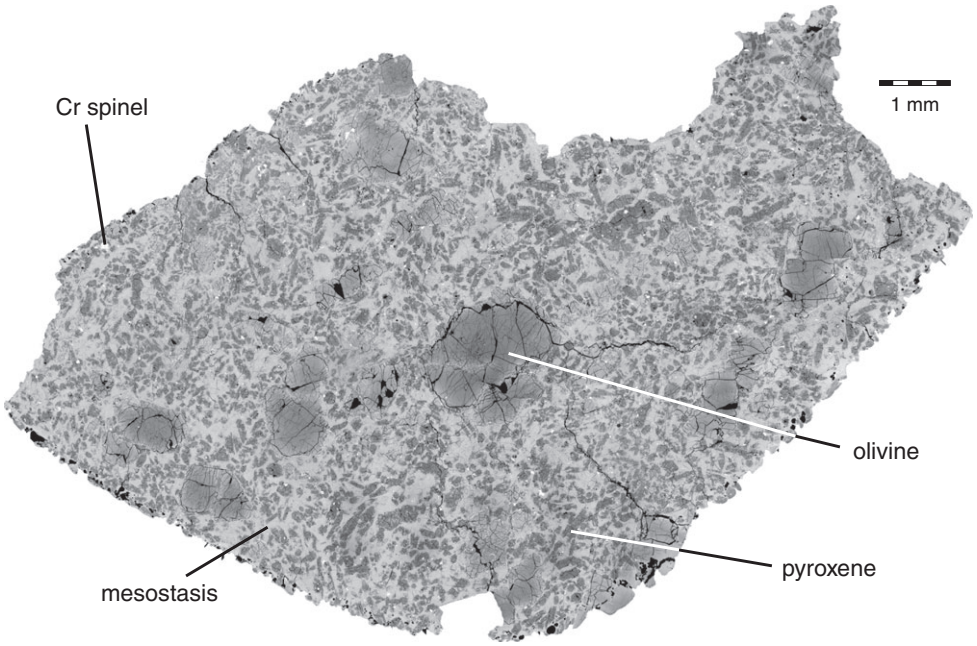

Fig. 1. BSE mosaic image of Y-980459 thin section with key phases labeled. The light gray mesostasis hosts olivine and pyroxene dendrites and sulfide droplets, most of which are not visible at this magnification.

arriving at cooling rates tailored to specific domains within the sample. For example, cooling rate estimates for phenocryst phases in Y-980459 range 0.03–5 °C h^{-1} for olivine phenocrysts (Greshake et al. 2004; Mikouchi et al. 2004; Miyamoto et al. 2009a) and 3–7 °C h^{-1} for pyroxene phenocrysts (Lentz and McSween 2005).

We performed dynamic crystallization experiments using the Y-980459 bulk composition as a starting material to critically evaluate whether these suggested cooling rates produce the crystal textures and compositional variations in the meteorite. Experimental time-temperature paths (Fig. 2) were assessed for applicability to Y-980459 using a tiered set of match criteria, in order from most to least stringent (1) phase assemblage, (2) modal proportions, (3) phenocryst texture, (4) phase compositions, and (5) groundmass crystal texture. Olivine morphology, quantitative textural analyses of pyroxene populations, and compositional analysis of glass and crystalline phases guided our determination of cooling rates. We then compared these estimates to a lava flow cooling model to constrain the depth within a flow at which Y-980459 cooled.

Suitability of Y-980459 for 1-Atmosphere Cooling Experiments

The whole-rock composition, and mineralogical and textural characteristics of Y-980459 make it exceptionally well suited for cooling rate evaluation via dynamic crystallization experiments. It lacks plagioclase/maskelynite and retains a primary glassy mesostasis, indicating final quenching on the surface of Mars. The bulk composition of Y-980459 is that of a magmatic liquid (Greshake et al. 2004; Ikeda 2004; Mikouchi et al. 2004; Musselwhite et al. 2006; Usui et al. 2008; Filiberto and Dasgupta 2011), obviating the need to calculate a liquid starting composition. Furthermore, constraints on the oxygen fugacity (fO_2) of the Y-980459 source are provided by valence-state-dependent partitioning of vanadium between olivine phenocrysts and melt (Shearer et al. 2006). It is possible for fO_2 to change during transit to and on the surface of Mars, but such a shift would have profound effects on the mineralogy of the meteorite. For example, at significantly more oxidizing conditions, Fe-Ti oxides containing Fe^{3+} would appear (e.g., Hammer 2006; Balta et al. 2013) and at significantly more reducing conditions, Fe metal would become stable. Neither titanomagnetite, metal blebs, nor reaction textures consistent with destabilization of primary silicate phases are present in Y-980459. Lacking direct evidence that fO_2 changed in the magma during transit to the Martian surface, for our experiments we adopt the ambient oxygen concentration corresponding to one log unit above the iron-wüstite redox buffer (IW+1) from Shearer et al. (2006).

The phase assemblage of the meteorite is relatively simple and well documented (Greshake et al. 2004; Ikeda 2004; Mikouchi et al. 2004; Usui et al. 2008),

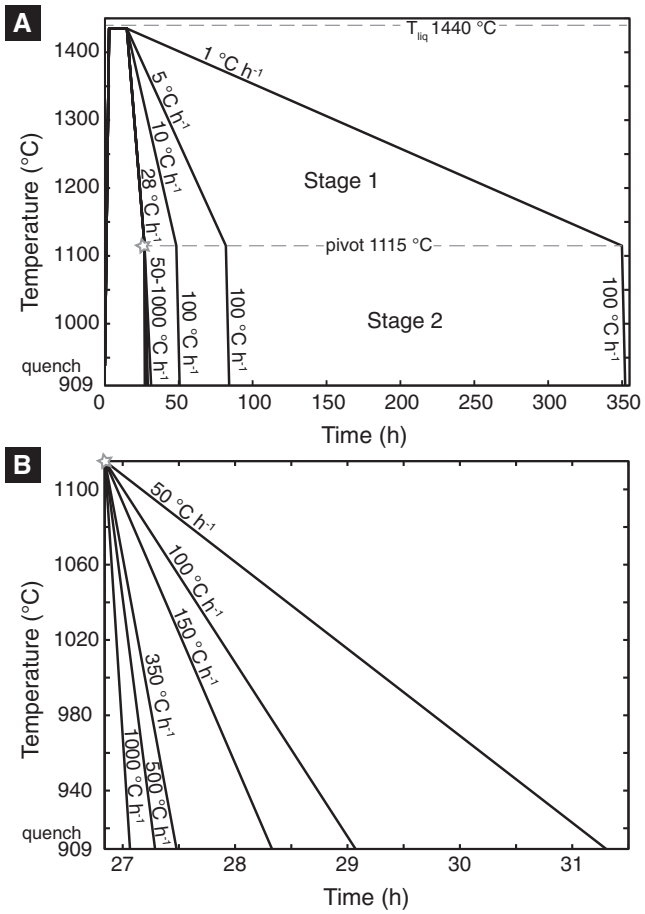

Fig. 2. Time–temperature paths for experiments listed in Table 2. A) Full experimental paths, emphasizing the HT series (Stage 2 = 100 °C h^{-1}). B) Enlargement, beginning at starred pivot point in (A), showing Stage 2 paths for the LT series (Stage 1 = 28 °C h^{-1}). The 28, 100 °C h^{-1} path is part of both series. See Table 2 for experiment names and details.

providing a robust set of metrics for evaluating experimental run products: 9–26 vol% of the meteorite consists of normally zoned olivine mega-phenocrysts with cores up to Fo_{85}, as well as smaller, more Fe-rich olivine phenocrysts (Figs. 1 and 3A). Prismatic pyroxene phenocrysts (48–58 vol%) are composed of low-Ca pyroxene rimmed by high-Ca pyroxene (Figs. 1 and 3A). The glassy mesostasis (23–37 vol%) contains olivine dendrites (Figs. 4A and 4C), with feathery and baby swallowtail morphologies (Donaldson 1976; Faure et al. 2003), and chain-like pyroxene. Minor phases include chromium-rich spinel grains, generally euhedral in shape, which occur as inclusions both in phenocrysts and in the groundmass glass. Sulfide (Fe, S, Ni) droplets are present in the mesostasis. Lamellar phosphorus enrichments in Y-980459 olivine crystals are reported by Shearer et al. (2013) and in this study (Fig. 5). Similar P enrichment patterns are recognized in an increasingly diverse set of olivine formation environments (e.g., Milman-Barris et al. 2008; Welsch et al. 2014; McCanta et al. 2016). The enrichments are spatially uncorrelated with major element compositional heterogeneity and have implications for initial crystal growth rate, as discussed below.

Phase equilibrium experiments performed at elevated pressure indicate that olivine is the liquidus phase of the Y-980459 composition up to 1.2–1.4 GPa (Musselwhite et al. 2006; Blinova and Herd 2009). The melt is multisaturated with olivine and low-Ca pyroxene at that pressure, suggesting this is the pressure at which Y-980459 melt equilibrated with a mantle mineral assemblage (Musselwhite et al. 2006; Blinova and Herd 2009). Furthermore, experimental olivine formed at ~1.2 GPa has a composition matching the most magnesian olivine ($Fo_{84–86}$) in the meteorite (Musselwhite et al. 2006), and thermobarometry (Lessel and Putirka 2015) supports the experimental results. The nominally anhydrous character of the shergottites, in general, and Y-980459, in particular (e.g., Usui et al. 2012), has the consequence of imparting relative insensitivity of pressure to the magmatic phase relations. This factor, coupled with the ability to finely control fO_2 and maximize sample size, justifies our 1-atmosphere investigation of crystallization dynamics in response to temperature change. With the understanding that absolute values of temperature scale upward with increasing pressure on the order of 20 °C per 100 MPa for a Y-980459 composition (Ghiorso and Sack 1995), the capability of our experiments to emulate crystallization processes occurring at depth in the Martian crust or mantle is supported by similarities in the phase appearance sequence and in mineral compositions, as detailed herein.

METHODS

Experimental Methods

Synthetic basalt with the composition of Y-980459 whole rock, hereafter termed Y98*, was created based on an S-free average of two published bulk analyses (Misawa 2003; Greshake et al. 2004) (Table 1). Practical impediments to working with S include difficulty maintaining fS_2, corrosion of the gas line supplying the furnace, and loss of S from the sample to holder materials. Given that S is a trace or minor element in this bulk composition (0.07–0.165 wt%; Table 1), its exclusion is unlikely to affect the phase assemblage (beyond the presence of a sulfide late in the crystallization sequence), silicate crystal morphologies, or liquid composition. Powdered oxide, carbonate, and phosphate reagents (SiO_2, TiO_2, Al_2O_3, Fe_2O_3, MgO,

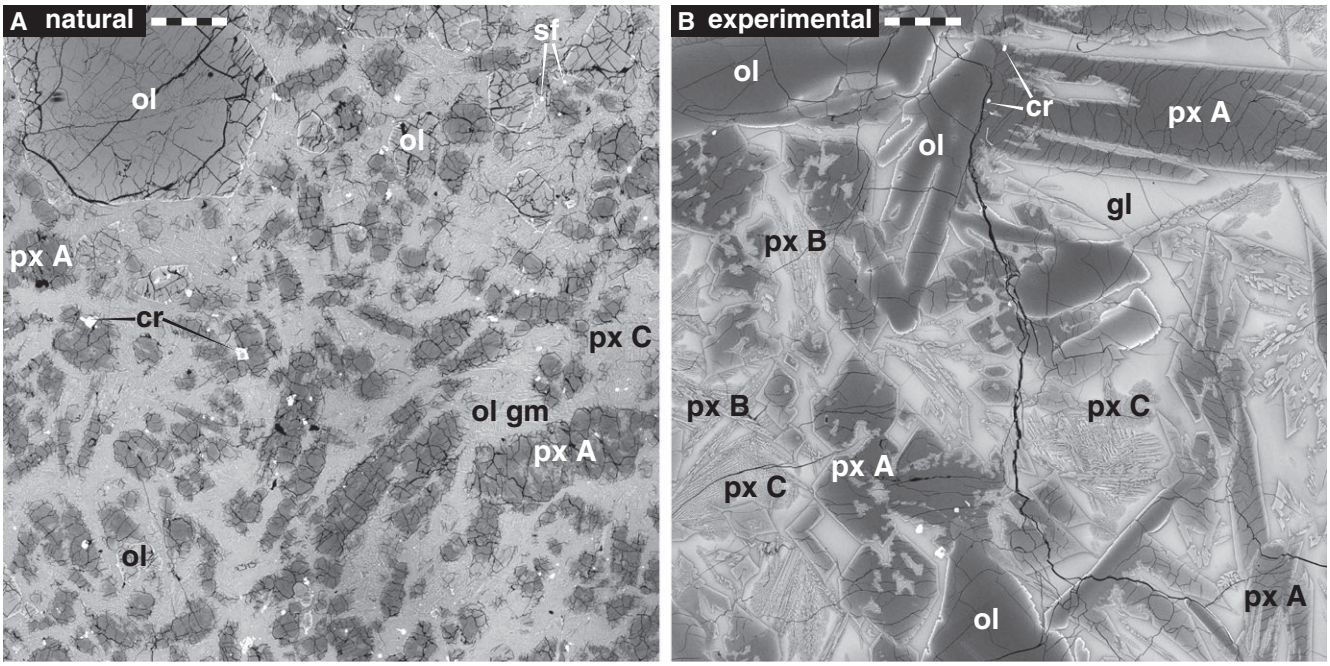

Fig. 3. BSE 100 × comparison of (A) meteorite and (B) experiment Y98*-f65. Scale bars are 250 μm. ol = olivine, ol gm = groundmass with olivine dendrites and glass, px A/B/C = pyroxene population A/B/C, cr = Cr-rich spinel, sf = sulfide, gl = glass.

Cr_2O_3, NiO, $CaCO_3$, Na_2CO_3, K_2CO_3, $MnCO_3$, $CaHPO_4$) were hand ground under ethanol for 5 h. The resulting homogeneous mixture was conditioned for ≥6 h at 925 °C under a flowing H_2-CO_2 gas mixture. These gases imposed an fO_2 approximately one log unit above the iron-wüstite redox buffer (IW+1), corresponding to formation conditions inferred for Y-980459 (Shearer et al. 2006). This conditioning drove off carbon and imparted the appropriate ferric-ferrous ratio. Charges were prepared by mixing the conditioned starting material with a polyvinyl alcohol solution to form a bead, inserting an Fe-Pt wire loop, and drying the prepared beads in a 50–60 °C oven for ≥30 min.

The Pt wire loop method (Presnall and Brenner 1974; Donaldson et al. 1975) limits Fe loss from silicate melt to Pt container by minimizing the amount of Pt in contact with the sample. However, reducing conditions exacerbate Fe loss by stabilizing a greater mole fraction of Fe in the resulting FePt alloy (e.g., Kessel et al. 2001). Because our experiments were all run at reducing conditions (corresponding to the IW+1 buffer), we used Fe-alloyed Pt wire loops. Each 2–4 mm diameter Pt wire loop was presaturated with Fe by electroplating and annealing (Grove 1981). Electroplating was conducted in a 23–25 °C bath of 25 g $FeSO_4 \cdot 7H_2O$ dissolved in 100-mL tap water, with high-purity Fe foil serving as the anode (Fig. S1 in supporting information). With currents of 45–50 mA, sufficient coating (approximately 20 wt% Fe preannealing) was achieved in 8–11 min per wire. Wires were then annealed in the gas mixing furnace at an fO_2 below the IW buffer for ≥3 h at 1500 °C, in order to ensure alloying of Fe and Pt metal. Postannealing wire compositions of ~17–18 wt% Fe substantially reduced iron loss to the container, as evaluated by comparing the glasses fused on Pt and various FePt wires using energy dispersive spectrometry (EDS).

Dynamic cooling experiments were conducted at atmospheric pressure in a DelTech gas mixing furnace at the University of Hawai'i at Mānoa (UHM), using flowing H_2 and CO_2 gases to control the sample environment (Fig. S2). Total linear gas flow rate was ~0.1 cm s^{-1}, consistent with methods in the experimental literature (e.g., O'Neill et al. 2003), and kept low to minimize loss of volatile elements Na and P from melt. Loss of Na is evaluated through quantitative analysis of matrix glass in experimental charges. P loss was not quantified, but was evidently not so extreme as to prevent uptake in rapidly grown olivine (Fig. S3). Time–temperature paths were set with a programmable Eurotherm controller. The removable experimental apparatus (Fig. S4) consisted of a double-bore alumina tube ("sample tube") run through with two ~1 mm diameter Pt wires ("quench wires"). Adjacent to the sample tube was a zirconia-based SIRO2 C700 + solid electrolyte oxygen sensor (error ±0.02 to ±0.04 log units of pO_2 according to the manufacturer; Ceramic Oxide Fabricators), calibrated to the IW buffer, wrapped with an external Pt sensor wire. A four-bore

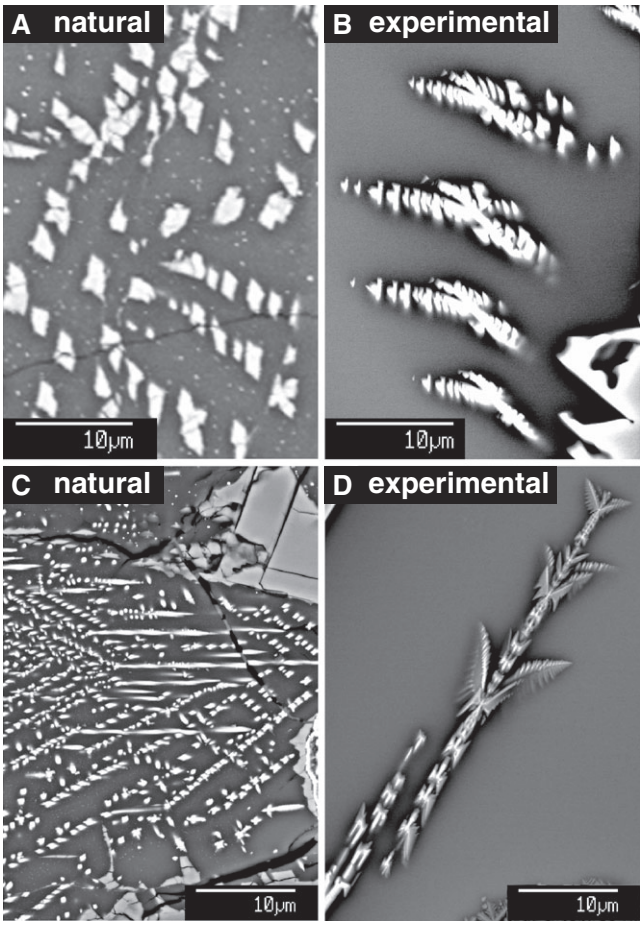

Fig. 4. BSE images of olivine dendrites. A, C) Y-980459; B) experiment Y98*-f65; D) experiment Y98*-f67. Note the morphological similarities between (A) and (B), (C) and (D). All images show dendritic crystals intersecting the section plane multiple times.

alumina tube, inside the sensor tube, housed the Pt electrode and wire and a Pt-Rh S-type thermocouple (error ±2.3 to ±3.6 °C according to the manufacturer; Omega Engineering). The internal four-bore tube also provided the conduit for a regulated flow of pure air to ensure known oxygen concentration at the reference electrode. One or two half-inch SALI-type alumina fiber baffles just smaller than the inner diameter of the furnace surrounded the sample and sensor tubes roughly one-third of the way up the apparatus. These baffles served to ensure complete and timely mixing of the gases. Late in our study, the apparatus was modified to include a third, thinner quench wire to allow for two separate quenches per run (Fig. S4).

Wire loop experiments were conducted as either single- or multi-bead runs, often employing a Pt wire "chandelier" for up to four beads (Fig. S4). The apparatus was inserted into the furnace at a hot-spot temperature of 938 °C, over approximately 6 min, to reduce the probability of thermal cracking of the sensor tube. A ramp rate of 3 °C min^{-1} was used to reach the desired starting temperature of the experiment. Oxygen fugacity was maintained at IW+1 ± 0.1 log_{10} units over the course of each experiment. Larger excursions occurred for brief (<1 min) periods. Below ~1050 °C, inefficient gas mixing caused some longer excursions in the reducing direction, mitigated by manually decreasing H_2 gas flow.

Samples were quenched into 100–200 mL of water by melting the quench wires with electric current (e.g., Edgar 1973). Because the water flask was attached to the furnace tube by a gas-tight seal (Fig. S5), a closed system was maintained throughout the quench. Quench crystals were not observed in any charges. For double quench experiments, we quenched one sample earlier in the run and another at the end, obtaining a snapshot at an intermediate time point.

Preparatory Experiments

More than 50 experiments were conducted to explore relevant experimental parameter space in reconnaissance fashion (Table S1). These runs, summarized below, helped to bracket mineral-in temperatures, establish precooling dwell conditions, evaluate the use of one versus two cooling rates, determine cooling rates necessary for plagioclase suppression, and select the experimental quench temperature. Many of these early experiments used pure Pt wire and lost Fe from the sample to the wire. Although the compositions of olivine and pyroxene were likely affected, the plagioclase appearance temperature and the rates of crystal nucleation and growth are considered less sensitive. Beads suspended from Pt and FePt wires run with an identical two-stage time–temperature path produced the same phase assemblage and texture (Fig. S6).

Through a series of eight isothermal runs of ≥6 h each, the Y98* liquidus temperature was determined as 1440 ± 2 °C, with olivine as the liquidus phase. Two additional isothermal experiments bracketed the equilibrium plagioclase-in temperature between 1120 °C and 1133 °C (Fig. S7). Super-liquidus treatments, intended to homogenize the starting material, resulted in unnatural textures upon cooling (single pyroxene crystal branching across the entire charge, Fig. S8). Since the physical relevance of superheating is inferred to be minimal (e.g., Lofgren 1980; Hort et al. 1999), and the textures were markedly different from the material we wished to replicate, a precooling dwell temperature of ~5 °C below the liquidus was implemented. Dwell periods of 12 and 24 h produced negligibly different outcomes (Fig. S9), and the shorter

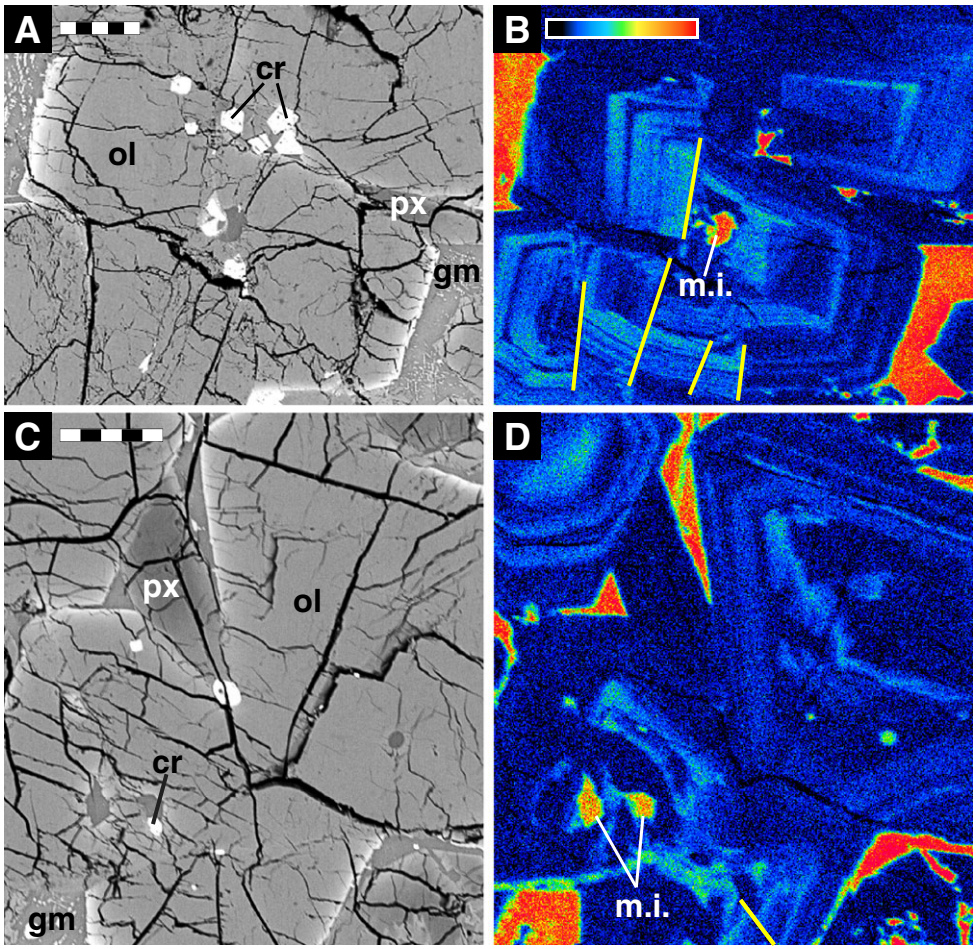

Fig. 5. BSE images and phosphorus X-ray distribution maps from two smaller Y-980459 olivine crystals. A) BSE image of crystal ol5; scale bar is 50 μm. B) Phosphorus X-ray map of crystal ol5; scale as in (A); on qualitative color scale, red is high and blue is low. Yellow lines highlight offsets in phosphorus zoning attributed to cracks visible in BSE. We interpret these cracks to have formed postcrystallization as the result of shock. C) BSE image of crystal ol8; scale bar is 50 μm. D) Phosphorus X-ray map of crystal ol8; scale as in (C); color scale and yellow lines as in (B). ol = olivine, px = pyroxene, cr = Cr-rich spinel, gm = groundmass, m.i. = melt inclusion.

time was adopted for subsequent runs. Single-rate cooling experiments, in which temperature was decreased from near the liquidus to 900–1000 °C at rates of 36 °C, 72 °C, and 320 °C h^{-1} failed to produce groundmass pyroxene, or produced barred pyroxene, or both (Fig. S10). Single constant-rate cooling was, therefore, unable to reproduce a key feature of Y-980459: at least two generations of morphologically distinct pyroxene crystals (as detailed below).

Two-stage cooling, utilizing two constant-rate cooling ramps changed at a pivot temperature, was explored next. A pivot temperature of 1115 °C, or 5 °C below the lower bracketing value for the equilibrium plagioclase-in temperature, was selected to separate the high-temperature Stage 1 cooling from the low-temperature Stage 2 cooling. This choice ensured that formation of feldspar was thermodynamically favored during the entire second stage of all experiments and permitted evaluation of cooling rate control on plagioclase nucleation behavior. A minimum Stage 2 cooling rate of 50 °C h^{-1} was adopted after observing plagioclase appearing in all runs at 36 °C h^{-1} and sporadically in runs with stage 2 cooling at 72 °C h^{-1}. Otherwise identical experiments quenched at 909 °C and 859 °C preserved no observable difference in texture (Fig. S11); all subsequent experiments were quenched at 909 °C.

Electron Microscopy

Every experimental charge was examined in backscattered electron (BSE) mode using the JEOL 5900 LV scanning electron microscope (SEM) in the W. M. Keck Cosmochemistry Laboratory at UHM.

Table 1. Bulk compositions in oxide wt%, modified from Brachfeld et al. (2015).

	Y98* bulk	Y-980459 bulk		NWA 5789 bulk	
	Experimental glass[a]	Greshake et al. (2004)	Misawa (2004)[c]	Gross et al. (2011)	Irving et al. (2010)
SiO_2	49.84	49.4	48.70	49.24	48.57
TiO_2	0.58	0.48	0.54	0.48	0.45
Al_2O_3	5.92	6.0	5.27	5.65	5.33
Cr_2O_3	0.67	0.71	0.71	0.46	0.73
FeO	17.85[b]	15.8	17.53	16.61	17.56
MnO	0.47	0.43	0.52	0.47	0.45
MgO	18.34	18.1	19.64	17.74	19.15
NiO	n.a.	0.03	0.034	0.03	0.0267
CaO	6.69	7.2	6.37	6.48	6.53
Na_2O	0.14	0.80	0.48	0.43	0.69
K_2O	0.01	0.02	<0.02	0.02	0.02
P_2O_5	b.d.	0.31	0.29	0.38	0.34
S	–	0.07	0.09	n.a.	n.a.
Total	100.51	99.35	100.17	97.99	99.85

[a]Synthetic Y-98* composition determined from the average of five electron microprobe analyses of a glass bead (f46i, Table S1). Low concentrations of alkali oxides and P_2O_5 are attributed to volatilization during fusion.
[b]Y-98* FeO value is an interpolation based on an FePt wire composition of 20% Fe, preannealing.
[c]Published wt% Ni and wt% FeS have been converted to wt% NiO and wt% S, with appropriate adjustment to wt% FeO.
n.a. = not analyzed, b.d. = below detection limit.

Analytical conditions were 15 kV accelerating voltage and 12 mm working distance. For most runs, images at 100× magnification were collected over the entire charge and later stitched together to form a composite image of the bead. Additional images at higher magnification were taken at points of interest, and electron-dispersive spectrometry (EDS) was used to confirm phase identities.

Experimental and natural phases were analyzed quantitatively using the JEOL Hyperprobe JXA-8500F electron microprobe at UHM, using Probe for EPMA software for all data output (e.g., Armstrong 1988; Donovan and Tingle 1996). Glass was analyzed over three sessions, with wavelength-dispersive spectrometry (WDS) spot analyses of Si (40–50 s on-peak counting time), Ti (30–50 s), Al (50–60 s), Cr (30–50 s), Fe (30 s), Mn (20–30 s), Mg (50 s), Ca (30 s), Ni (50 s, measured during one session only), Na (30 s, measured first), K (30–40 s), and P (30–50 s). High and low off-peak counting times were each half of on-peak times. For glass, an accelerating voltage of 15 kV and a beam current of 10 nA were used. The beam diameter was 10 μm or ≥5 μm for smaller areas of glass. Basaltic glass standards VG-A99 USNM 113498/1 and VG-2 USNM 111240/52 (Jarosewich et al. 1980) were measured periodically to ensure measurement fidelity and check for drift. Calibration was based on these basaltic glass standards (Si, Al, Fe, Ca), sphene glass (Ti), Verma garnet or rhodonite (Mn), chromite USNM 117075 (Mg, Cr), NiO (Ni), Amelia albite (Na), orthoclase (K), and fluorapatite USNM 104021 (P) standards. Background fits were linear for all elements. Phi-Rho-Z matrix corrections of Armstrong/Love Scott were applied. Detection limits and uncertainties were evaluated (Table S2).

WDS spot analyses of olivine and pyroxene were gathered over four sessions for Si (20–30 s on-peak counting time), Ti (30–40 s), Al (20–30 s), Cr (30–35 s), Fe (30–35 s), Mn (30–55 s), Mg (20–30 s), Ca (30–45 s), Ni (30–50 s), Na (20–30 s, measured first), K (25 s, measured for Y-980459 crystals only), and P (60–70 s, measured for Y-980459 crystals only). High and low off-peak counting times were each half of on-peak times. An accelerating voltage of 20 kV and a beam current of 20 nA were used for experimental crystals. Y-980459 olivine and pyroxene were measured with an accelerating voltage of 15 kV and a beam current of 25 nA (large crystals) or 15 nA (dendrites and rims). In all cases, beam diameter ranged from 10 μm (cores, large crystals) to focused (dendrites, rims). Springwater olivine USNM 2566 and Kakanui augite USNM122142 (Jarosewich et al. 1980) were measured periodically to ensure measurement fidelity and check for drift. Calibration was based on this olivine and pyroxene (Si, Al, Fe, Mg, Ca), sphene glass (Ti), chromite USNM 117075 (Cr), Verma garnet (Mn), NiO (Ni), Amelia albite (Na, Al), orthoclase (K), and fluorapatite USNM 104021 (P, Ca) standards. Background fits were linear for Si, Fe, Mg, Ca, Ni, and Na and exponential for Ti, Al, Cr, Mn, and P. Phi-Rho-Z matrix corrections of Armstrong/Love Scott were applied. Detection limits and uncertainties were evaluated (Tables S3 and S4). High-resolution BSE images were collected at 15 kV accelerating voltage.

Phosphorus X-ray distribution maps for two olivine crystals in Y-980459 were acquired with a 15 kV accelerating voltage, 100 nA beam current, 40 ms dwell time, and 0.5 μm step size. Two PET(H) crystals collected P kα X-rays. Map dimensions are 500 × 450–600 pixels.

Image Analysis

Point counts were made on composite BSE images, using at least 400 points per experimental charge and 916 points for the meteorite, employing the assumption that area fraction is equivalent to volume fraction when no fabric is present (Hilliard 1968). In the groundmass of Y-980459, areas of olivine versus pyroxene were distinguished in BSE images by the higher Z-contrast (i.e., greater Fe content) of the olivine dendrites in comparison with the pyroxene groundmass crystals. High-magnification images (500–2000×) were used to obtain the average volume fraction of each groundmass phase in an area of mesostasis composed of that phase and glass. This ratio of crystal to glass was applied to the relevant points of the original low-magnification point count, for which groundmass crystals were unresolvable from glass. For experimental samples, the same method was applied to 2000× magnification images from each run to determine the pyroxene-glass ratio for regions containing fine-grained pyroxene.

The surface area per unit volume (S_v^P) for pyroxene populations was determined using standard stereological image analysis techniques and detailed methodology of Hammer (2009). Measurements of S_v^P were used partly because they do not require knowledge of nucleation density. Metrics dependent on nucleation density (e.g., crystal size distribution) would provide less suitable characterizations of the crystal morphologies we studied, due to difficulty in distinguishing branches of one crystal from another and the possibility of broken crystals in the natural sample. By using S_v^P, texture was quantified in a way that is appropriate for both natural and experimental samples. The units of S_v^P are mm^2/mm^3 or simply mm^{-1}. Briefly, S_v^P of a phase is related to the number of intersections of that phase with a given length of test line (N_L) and the volume fraction of the phase (ϕ), as $S_v^P = 2\ N_L/\phi$ (Underwood 1968). Circular test lines were digitally drawn on BSE images at 75–100×, 250–1000×, or 2000×, depending on population type (defined below). Intersections of crystal edges with the test line were marked using Photoshop and counted using Image J (Schneider et al. 2012). Volume fraction was determined by thresholding or point counting the image area inside each individual test circle. For statistical purposes, we determined a sample size (n) for each test line, based on its length and the resolution of the image (included in the supporting information). Test line length was also used to derive weighted averages, combining individual measurements in proportion to their spatial relevance.

RESULTS

The two-stage dynamic cooling experiments fall into two series, the HT (high-temperature) series and the LT (low-temperature) series (Fig. 2), which explore the effects of initial cooling and low-temperature cooling, respectively, on mineralogy and texture. In the HT series, the high-temperature (Stage 1) cooling rate varied from 28 °C h^{-1} to 1 °C h^{-1} and the lower temperature (Stage 2) cooling rate was held constant at 100 °C h^{-1}. In the LT series, Stage 1 was held constant at 28 °C h^{-1} and Stage 2 was varied from 1000 °C h^{-1} to 50 °C h^{-1}. For experiments discussed henceforth (Table 2), each run consisted of two sample beads run simultaneously on separate FePt alloy wire loops. No differences were observed between beads, unless otherwise noted, indicating general reproducibility of textural and compositional outcomes. The supporting information contains full-bead BSE images of each run (Fig. S12).

Textures

Descriptive

Every experimental sample contains all phases present in Y-980459, except sulfides (Table 2). Olivine phenocrysts in the LT series are large (1 mm range), have Fe-rich rims where in contact with glass, and exhibit skeletal morphologies. In the HT series, olivine phenocrysts are similar (Fig. 3B), but the degree of infilling increases with decreasing Stage 1 cooling rate. Two beads (one each from Y98*-f57 and Y98*-f63) contain small polyhedral olivine grains (~100 μm), clustered at the base of the charge (Fig. S13). However, no run products contain large, euhedral olivine grains resembling those in Y-980459.

Olivine dendrites or dendritic overgrowths formed in all runs in both series. Their morphologies are feathery, chain-like, or swallowtail in nature (Fig. 4B, Fig. 4D). Although these shapes are similar to those observed in the meteorite (Fig. 4), the olivine dendrites in experiments are less volumetrically abundant than those in Y-980459.

Cr-rich spinel occurs throughout experimental samples and grains are especially prevalent on FePt wires. Spinel crystals from the HT series are euhedral, whereas some in the LT series are skeletal. In HT runs <28 °C h^{-1}, Cr-spinel crystals reach ~100 μm in diameter. This grain size is larger than all but one

Table 2. Experimental run information[a] and selected results.

	Sample Y98*-	Cooling rate (°C h^{-1})		Modal mineralogy (vol%)							Crystallinity (φ)		Surface area per unit volume (mm^{-1})		
		Stage 1	Stage 2	Olivine		Cr-spinel	Pyroxene			Glass	Point count	K_2O	Pyroxene		
				Phenocryst	Dendrite		Pop A	Pop B	Pop C				Pop A	Pop B	Pop C
LT	f63	28	1000	19.8	tr.	0.4	36.3	0.8	3.0	39.6	0.60	0.59	95	1752	9178
	f56	28	500	29.7	tr.	tr.	30.1	0.8	3.4	36.0	0.64	0.58	89	1922	8649
	f67	28	350	20.7	tr.	tr.	38.1	2.7	7.5	31.0	0.69	0.69	65	1801	7123
	f57	28	150	18.2	tr.	tr.	37.1	10.7	1.0	33.1	0.67	0.51	89	1181	6672
	f64[b]	28	50	17.9	tr.	0.4	42.9	2.9	0.9	17.2	0.83	0.63	n.a.	n.a.	n.a.
LT&HT	f62	28	100	20.6	tr.	0.2	39.5	6.2	1.4	32.0	0.68	0.65	81	1295	5643
HT	f65	10	100	22.5	0.2	0.2	42.7	6.8	1.7	26.0	0.74	0.65	49	1169	6778
	f68	5	100	16.1	tr.	1.0	46.4	2.9	3.9	29.8	0.70	0.49	40	1882	5404
	f69	1	100	16.6	tr.	tr.	41.0	1.4	1.6	39.5	0.61	0.34	25	1657	5159
	f69[c]	1	100	1.7	tr.	0.7	39.2	0.7	2.8	53.5	0.47	0.26	n.a.	n.a.	n.a.
	Y-980459[d]	–	–	19.7	1.9	0.7	49.8	–	4.6	23.4	0.77	0.66	46	–	6477

[a]For all runs, an initial 12 h subliquidus dwell between 1428 and 1435 °C preceded cooling. All pivot temperatures between Stage 1 and Stage 2 were between 1111 and 1116 °C, below the equilibrium plagioclase-in temperature. All quench temperatures were 909 °C. For preparatory experiments, see Table S1.

[b]Y98*-f64 contains 17.9 vol% intergrown plagioclase and pyroxene.

[c]Y98*-f69 (bead ii) contains 1.4 vol% cristobalite.

[d]Y-980459 contains sulfides, though none fell on intersections for the point count.

tr. = trace, n.a. = not analyzed.

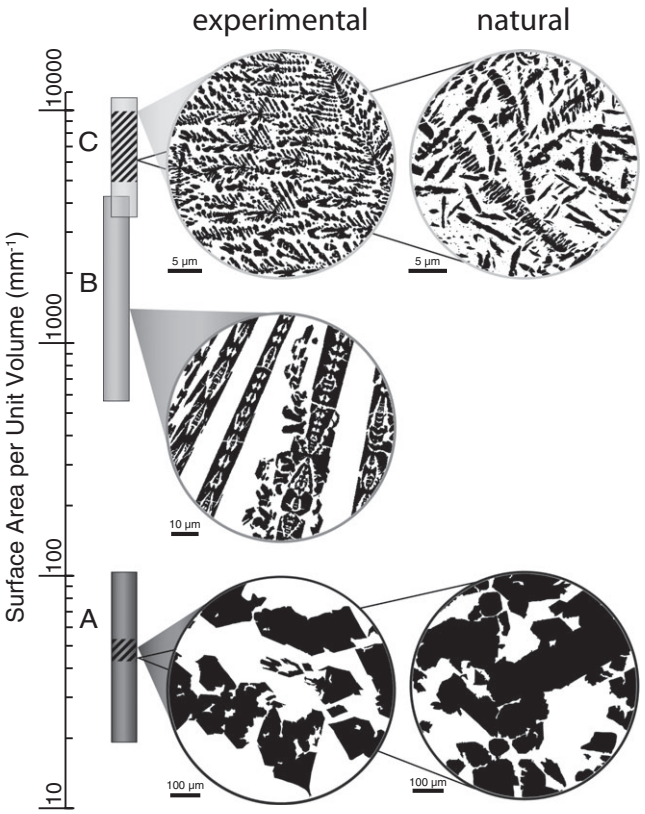

Fig. 6. Summary of surface area per unit volume for experimental and natural pyroxene populations. Shaded vertical bars show experimental ranges exhibited by crystals of each of three populations, A, B, and C, described in the text. Ranges exhibited by meteorite crystal populations are indicated as subsets with diagonal striping. Binary images representative of each population in the experimental and natural samples are shown at right, with cones indicating the corresponding S_v^P value for each image.

Cr-spinel crystal in Y-980459, in which most are 30–50 μm in diameter.

The experimental pyroxene crystals are qualitatively divided into three populations (A_e, B_e, and C_e), using criteria based on size, morphology, and atomic number contrast in BSE images (Fig. S14). Population A_e (Figs. 3B and 6) consists of phenocrysts with Mg-rich cores and Ca- and Fe-rich rims, with some patchy zoning. These crystals are typically elongate and externally faceted, with numerous embayments and interior melt inclusions. Among the HT runs, more infilling occurs with decreasing Stage 1 cooling rate. Smaller crystals with faint to no zoning are nearly equant, with a combination of facets and sparse embayments. In the HT series, the abundance of population A_e peaks at 5 °C h^{-1}.

Population B_e (Figs. 3B and 6) consists of smaller crystals, generally chain-like, some of which branch off from phenocrysts. These chains are H-shaped or lantern-like (Bryan 1972; Donaldson 1976), occasionally occurring as isolated crosses. Population B_e is compositionally unzoned, with a similar or higher average atomic number than the rims of population A_e pyroxenes.

Population C_e (Figs. 3B and 6) comprises the smallest segments. These crystals are dendritic, finely branching or radiating, and are the most Fe rich. A glassy boundary layer typically separates phenocrysts from population C_e crystals. Populations B_e and C_e are absent from samples quenched at the end of Stage 1 (Fig. S15), indicating that they formed during Stage 2. The abundances of both of these populations peak at intermediate cooling rates in both series.

Y-980459 contains two pyroxene populations, A_n and C_n, analogous to populations A_e and C_e. There is no population B_n in the meteorite (see the Discussion section). Population A_n is morphologically similar to population A_e (Figs. 3A and 6), but crystals tend to be smaller, with a higher number density. Population C_n (Figs. 3A and 6) comprises groundmass crystals that are elongate and micron-scale, similar to those in population C_e. However, C_n crystals cover a continuum of sizes and are chain-like, but blocky. They are infilled and segmented, with fewer branches than population C_e crystals.

Minerals not occurring in Y-980459 formed in two experiments. Plagioclase crystallized in Y98*-f64. Cristobalite (as determined by Raman spectroscopy and provided in the supporting information) crystallized in one bead of Y98*-f69 (Fig. S16). Paradoxically, the cristobalite-bearing bead has the lowest overall crystallinity ($\Phi = 0.47$) but highest glass SiO_2 content (55 wt%) of all beads analyzed. Cristobalite also appeared in an earlier run with the same *T-t* path (Y98*-f66, Table S1), indicating reproducibility. Cristobalite is not present in the bead quenched at the end of Stage 1 in run Y98*-f66 (Fig. S15C), suggesting that it formed during Stage 2. The presence of this unexpected mineral hints at kinetic effects during the longest run and is considered in the Discussion section.

The overall crystallinity of the LT series increases linearly from $\Phi = 0.68$ as Stage 2 cooling rate decreases (Table 2), except for one anomalously crystalline run (Y98*-f67). This trend is consistent with slower low-temperature cooling allowing more time for crystal nucleation and growth. In the HT series (Table 2), crystallinity peaks at 10 °C h^{-1} ($\Phi = 0.74$), suggesting that the combined rates of nucleation and growth are maximized at intermediate cooling rates. Compared to the meteorite ($\Phi = 0.77$), experimental samples with the correct phase assemblage are less crystalline ($\Phi = 0.60$–0.74).

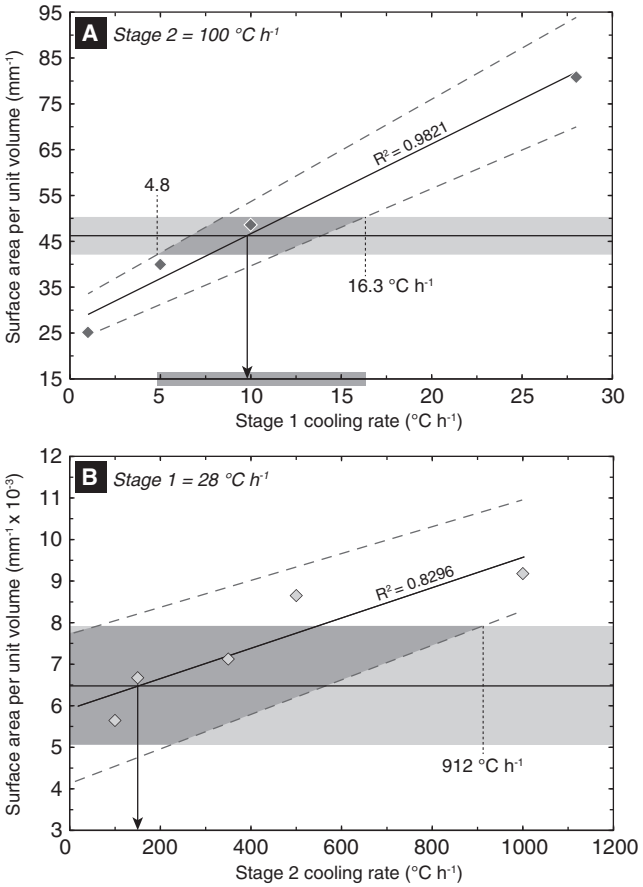

Fig. 7. Surface area per unit volume of pyroxene populations. A) population A; least-squares regression line fit to experimental (population A_e) weighted averages plotted as a thick line; least-squares fits to 1 σ variances plotted as dashed lines; meteorite (population A_n) weighted average plotted as horizontal black line, with 1 σ variance shown as shaded band. The intersection of this horizontal band with the region between the dashed lines represents the range of cooling rates possible for natural pyroxene population A, within error. B) population C; lines and shading equivalent to those described in (A).

Surface Area Per Unit Volume Measurements

The qualitative division of pyroxene crystals into populations is substantiated by calculated surface area per unit volume (S_v^P; Fig. 6, Table S5). Population ranges are distinct, with little overlap between populations B_e and C_e. In the LT series, the S_v^P of population A_e increases slightly with Stage 2 cooling rate (Table 2), although Y98*-f67 contradicts this trend, with a lower S_v^P than expected. (This run is also more crystalline, pointing to favorable nucleation and/or growth conditions.) In the HT series, the weighted average S_v^P of population A_e increases linearly with Stage 1 cooling rate (Fig. 7A). Including the standard deviations of both A_n and A_e, the meteorite population overlaps the experimental S_v^P values between 5 and 16 °C h^{-1} (Fig. 7A). The weighted average S_v^P of A_n (46 mm^{-1}) intersects the trend for the HT runs near Stage 1 = 10 °C h^{-1} (Fig. 7A).

The S_v^P values of population B_e and C_e pyroxenes do not change coherently within the HT series (Table 2), suggesting formation during Stage 2. In the LT series, the weighted average S_v^P of population C_e consistently increases as Stage 2 cooling rate increases (Fig. 7B). Population C_n has a weighted average S_v^P of 6500 mm^{-1}, intersecting the LT experimental trend at a Stage 2 cooling rate near 150 °C h^{-1} (Fig. 7B).

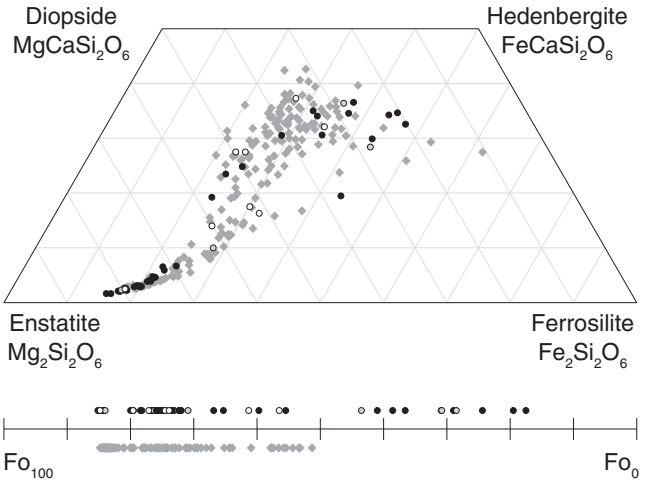

Fig. 8. Pyroxene and olivine endmember compositions. Gray diamonds are experimental data points, and circles are Y-980459 data points. Meteorite data from this study (black), plus representative analyses from Greshake et al. (2004) (light gray) and Usui et al. (2008) (white).

Phase Compositions

Pyroxene crystals from the LT and HT series span a large compositional range, from En_{80} to En_{11} (Fig. 8). They evolve from magnesian to ferroan and from low Ca to higher Ca. Population A_e crystals fall mainly at the high En end, and smaller crystals have lower En contents. To a first order, this range is independent of cooling history, as demonstrated by the overlap within both the LT and HT series (Fig. 9; Table S3). Experimental pyroxene crystals span approximately the same compositional range as Y-980459 pyroxene crystals (Fig. 8).

In Y-980495 and both experimental series, pyroxene compositions cluster tightly at the high-MgO end of the spectrum, fanning out to larger scatter below 23 wt% MgO (Fig. S17). This divergence point also corresponds to about 1.5 wt% Al_2O_3, 4 wt% CaO (Fig. S17), and is reflected in the stoichiometric components (Fig. 8). Pyroxene cores extend to slightly higher MgO contents

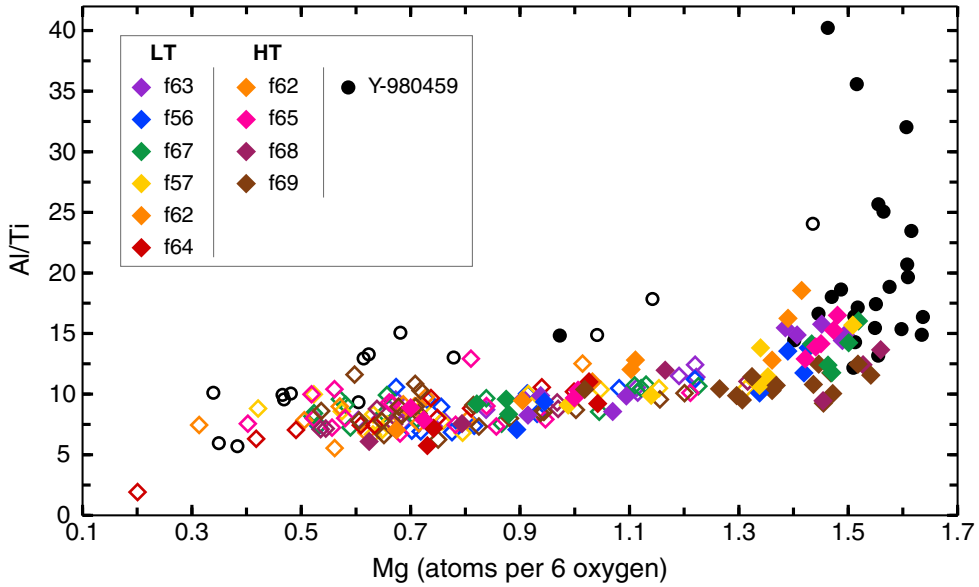

Fig. 9. Pyroxene compositions, presented as Al/Ti ratio versus atomic Mg. Filled shapes represent cores; open shapes represent rims. Experimental analyses plotted as diamonds; Y-980459 plotted as circles. Error within symbol size.

in Y-980459 (maximum 31.71 wt% MgO) than in experiments (maximum 29.11 wt% MgO). Pyroxene crystals in Y-980459 contain less TiO_2 than those of experiments (Fig. S17), consistent with the higher TiO_2 content of a subset of the meteorite Fe-Ti oxide crystals (Brachfeld et al. 2015). This low TiO_2 causes the Al/Ti trend in Y-980459 to be slightly higher than that defined by experiments (Fig. 9). Mg-rich natural pyroxene analyses extend to much higher Al/Ti (Fig. 9).

Pyroxene crystals in the meteorite extend to higher Na_2O contents than those in experiments (Table S3), as expected given the higher glass Na_2O in Y-980459 (Fig. S18B). Cr_2O_3 in meteorite pyroxene is ≤1.05 wt%, whereas in experiments, many grains contain higher Cr_2O_3 (Table S3). Small differences in Cr-spinel abundance can explain this result. Indeed, pyroxene compositions in experiments with lower Cr-spinel abundance than Y-980459 (Table 2) extend to 1.7 wt% Cr_2O_3, whereas those with higher Cr-spinel abundance (Table 2) contain pyroxene more similar to the meteorite, reaching only 1.1 wt% Cr_2O_3. The differences noted above are minor. In general, compositional similarity between pyroxene in Y-980459 and the experimental set was achieved.

The composition of experimental olivine is similarly uncorrelated with cooling history for both LT and HT runs. Olivine core compositions in experiments (37.86–44.78 wt% MgO) and Y-980459 (38.13–45.81 wt% MgO) largely overlap (Fig. 8, Fig. S19). One apparent mismatch is the lack of experimental rim or dendrite analyses more Fe rich than Fo_{51}, compared with Y-980459 olivine as ferrous as Fo_{18} (Fig. 8). Natural trends extend to higher FeO and MnO and lower MgO and SiO_2 (Fig. S19). Given the scarcity of olivine dendrites in experiments, and the difficulty of analyzing their submicron branches, the discrepancy is partly a sampling bias. However, the high crystallinity of the meteorite (Φ = 0.77) also suggests that the melt of Y-980459 would have had a lower MgO/FeO ratio at the time of dendrite formation, compared with experiments (Φ = 0.6–0.74). This is supported by the meteorite's more evolved residual glass compositions (Fig. 10).

Glass compositions in this study are more sensitive to experimental cooling history than crystal compositions. As Stage 2 cooling rate decreases, LT glasses are richer in Al_2O_3 (Fig. 10A), but poorer in MgO and CaO (Fig. 10B), consistent with increasing crystallinity (Table 2). Conversely, in the HT series, the two fastest cooling rates produced glasses with lower MgO and CaO than those of the two slowest cooling rate experiments (Fig. 10C). This counterintuitive result is reflected in the crystallinity of the samples; the slowest-cooled experiment is the least crystalline (Table 2). The residual glass of Y-980459 is comparatively more evolved, in that it generally contains less MgO, less CaO, and more Al_2O_3 than experimental glasses (Fig. 10). The experiment that comes closest to matching the 0.74 wt% MgO glass average for the meteorite is Y98*-f65 (1.97 wt% MgO). Y98*-f65 is also the closest match to the glass CaO and Al_2O_3 values in Y-980459. The glass in Y-980459 has higher average Na_2O and K_2O than any experimental glass (Fig. S18), an inferred result of experimental Na

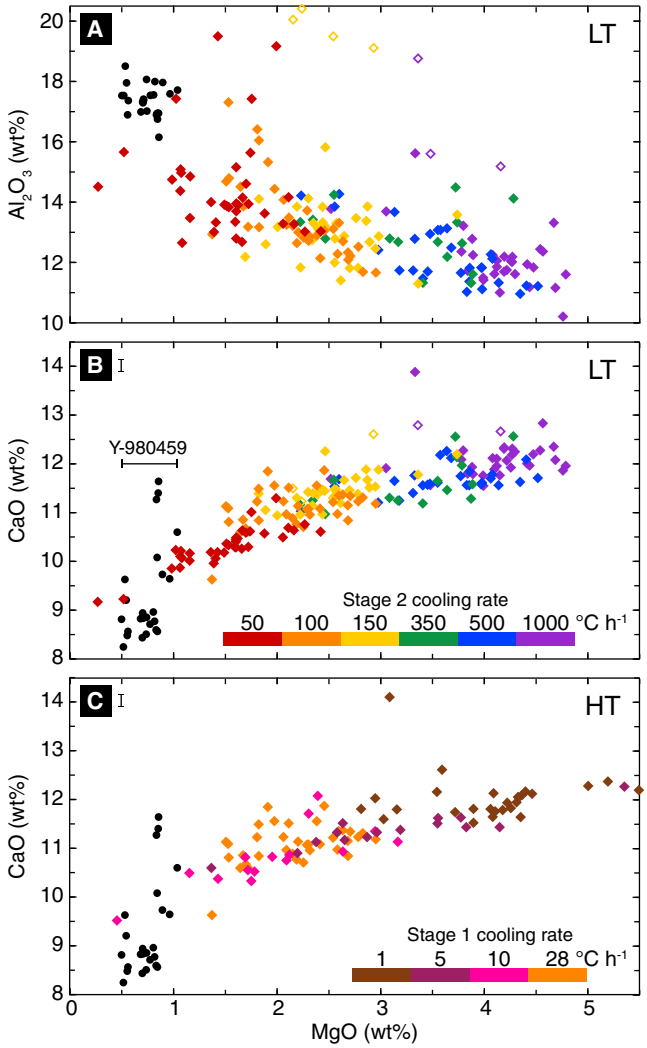

Fig. 10. Glass compositions. Experimental data plotted as diamonds, meteorite plotted as black circles. Legend in (B) also applies to (A), and horizontal axis applies to all plots. Error bars within symbol size are shown at top left. A) Al_2O_3 versus MgO for the LT series. Open diamonds for Y98*-f57 and Y98*-f63 represent analyses of interstitial glass from areas of closely packed olivine crystals, analogous to an intercumulus melt. B) CaO versus MgO for the LT series. C) CaO versus MgO for the HT series.

loss during the initial high-temperature dwell (Table 1) and differences in crystallinity.

DISCUSSION

Controls on Phase Composition and Mode

The experiment-meteorite overlap in olivine and pyroxene compositions provides evidence for broadly similar crystallization conditions. The reason for discrepancies in glass composition between Y-980459 and many experiments is, therefore, not immediately apparent. For example, taking the LT and HT series together, olivine and pyroxene reach similar maximum and minimum CaO and Al_2O_3 as their counterparts in the meteorite (Tables S3 and S4). However, glass in Y-980459 contains more Al_2O_3 and less CaO (on average) than experiments (Fig. 10). Thus, it is the amount of each mineral composition that differs between the meteorite and experiments, not the presence or absence of a particular composition. Rather, glass compositions, modal analyses, and textural properties of each sample are better suited to preserving cooling history.

The tight-to-scattered trend in LT, HT, and natural pyroxene compositions (Fig. 8) may be a hallmark of disequilibrium crystallization. Pyroxenes from several other shergottites also exhibit greater heterogeneity at higher Fs and/or Wo contents (QUE 94201 and EETA 79001, Mikouchi et al. 1998; NWA 480, Barrat et al. 2002a, 2002b; NWA 5789, Gross et al. 2011; Tissint, Balta et al. 2015). Notably, the scattered analyses are made up largely of rims and nonphenocryst populations. In this study, we interpret this pattern as an indication of greater melt inhomogeneity at the faster cooling rates (Stage 2) during which these pyroxene subsets formed. Rapid cooling places kinetic limitations on the ability of species to diffuse through the melt (Albarede and Bottinga 1972), creating a chemically inhomogeneous melt and corresponding inhomogeneous crystal population. Disequilibrium conditions appear to have affected the trace element compositions of even the pyroxene phenocrysts in Y-980459 (Usui et al. 2008), so with subsequent faster cooling, it is logical that the consequences of disequilibrium are more pronounced. Similar kinetic effects may have played a role in pyroxene crystallization for other shergottites, though the initial cause (rapid cooling, high undercooling, etc.) may vary.

In pyroxene analyses with less than ~1.6 Mg cations per six oxygens, the higher Al/Ti ratios in Y-980459 crystals compared with experimental crystals (Fig. 9) are attributed to crystallization from a liquid slightly more depleted in Ti. The meteorite contains spinel grains with higher Ti contents than any in the experiments (Brachfeld et al. 2015), providing a mechanism whereby the natural liquid evolved with lower Ti. For the most Mg-rich meteorite pyroxene analyses, however, the Al/Ti ratio is highly variable and extends to values far too large for this explanation to be reasonable. These high values represent population A_n only and may reflect initial pyroxene crystallization at higher pressures, which would stabilize the jadeite component at the expense of the diopside and enstatite components (Putirka et al. 1996). This interpretation is in keeping with the positive Al_2O_3-Na_2O correlation present in Y-980459 pyroxene crystals (Table S3). A high-pressure interpretation is

consistent with the Al/Ti pressure calibration reported in Nekvasil et al. (2004), but like Balta et al. (2015), we are cautious about placing numerical constraints on formation pressures of Y-980459 crystals based on experiments using an alkalic composition.

Kinetic effects may have influenced K_2O-based crystallinity calculations. For Y-980459, HT, and LT samples, the crystallinity calculated using glass K_2O content is consistently lower than point-counted crystallinity (Table 2). Thus, either perfect incompatibility is not an accurate assumption or the full extent of glass heterogeneity was not captured by spot analyses. In Y-980459, K_2O was detected in 11 of 122 FeMg silicate analyses, at ≤0.04 wt%. Adding this K_2O back to the melt does not reproduce the point-counted crystallinity value, indicating that compatibility of K_2O cannot fully explain this discrepancy. Generally, we obtained analyses away from potential boundary layers, aiming for the largest and most homogeneous melt pockets. However, boundary layers around growing crystals are typically enriched in incompatible elements (e.g., Albarede and Bottinga 1972; Lasaga 1982). Milman-Barris et al. (2008) report K_2O enrichment of ~30% measured within 250 μm of olivine crystals in their experimental charges. Boundary layers are indeed visible in BSE images of Y-980459 and our experimental suite (Fig. S20), and these unanalyzed regions could explain the apparent low glass K_2O content of samples. Additionally, olivine and pyroxene dendrites too small to measure grew rapidly and may have incorporated higher concentrations of normally incompatible elements from these boundary layers (e.g., Welsch et al. 2013), including K. Thus, we take point counts as the more accurate measure of sample crystallinity.

Interpreting Population C

Population C crystals generally have a wide range of S_v^P values within a given sample, including individual measurements up to 1.5 times higher than the weighted average, in both Y-980459 and experiments. One explanation for these high values is that crystal growth typically begins rapidly in response to a perturbation in the degree of undercooling (e.g., Dowty 1980), such as an abrupt increase in cooling rate. Thus, some high S_v^P values would be expected at every Stage 2 cooling rate. However, following the perturbation, growth rapidly decays to a lower rate, shutting down dendritic growth. Slower cooling affords more time for crystals to infill and produce morphologies consistent with slow growth. Crystal populations with short growth windows may, therefore, capture both incipient and slightly more developed stages of crystallization. Thus, the brief growth interval of population C crystals promotes much greater variation in S_v^P (Fig. 7B) than is seen for crystal populations grown over longer time periods. For example, population A grew for long enough that the quasi-steady-state growth rate eclipsed any transient rapid growth initially following nucleation. Despite the variation in the data, the weighted average S_v^P of population C_e in each sample shows a clear dependence on cooling rate and is viewed as a viable constraint.

The nature of this smallest population also indicates minor discrepancies between Y-980459 and experiments. The highly branching and locally concentrated C_e pyroxenes (Fig. 6) contrast with the blockier, evenly distributed C_n microlites (Fig. 6). We examine two explanations for these differences: flow-induced strain and higher pivot temperature or a combination of these. These processes could also explain the scarcity of olivine dendrites in experiments.

First, flow is an important natural process not simulated in this study. Experimental work on basalt (Kouchi et al. 1986; Vona and Romano 2013) indicates a negative correlation between strain rate and nucleation incubation time. Essentially, flow promotes a greater nucleation density of microlites than does stagnation (up to 10× more; Kouchi et al. 1986). Field studies also invoke mechanical stirring as an explanation for the high crystallinity of particularly microlite-rich lavas (e.g., Macdonald 1953; Cashman et al. 1999; Hon et al. 2003). If Y-980459 crystallized while flowing, strain may have induced a greater nucleation density across the entire groundmass. This strain also could have broken apart fragile, branched crystals, scattering pieces of the crystals throughout the melt. These effects of flow may explain the presence of more individual groundmass crystals distributed throughout Y-980459, contrasted with the spatially restricted pockets of more branching crystals in experiments.

Second, the pivot temperature between the equivalent Stage 1 and Stage 2 cooling rates in the meteorite may have been different than that used in our experiments (1115 °C). We ascertained that a lower pivot temperature would likely result in plagioclase formation during Stage 1 (Fig. S7). However, the upper bound is unconstrained. If Y-980459 began Stage 2 cooling at a higher temperature, the thermodynamic driving force for nucleation would be greater, because the undercooling would be larger. Thus, a combination of flow and higher pivot temperature may explain the more uniform spatial distribution and apparent higher nucleation density of the natural groundmass crystals.

Missing Population B_n

The absence of a population B_n in Y-980459 is interpretable within the framework of nucleation and

growth theory (Kirkpatrick 1981). The number density of population A_e is less than that of population A_n, and A_e crystals are generally larger. This indicates that during Stage 1 cooling, nucleation in experiments was somewhat inhibited relative to the natural magma. Thus, individual experimental crystals grew larger, as there was less surface area on which growth could occur. The initiation of rapid cooling (Stage 2) and relative scarcity of growth substrate promoted nucleation of two new experimental populations (B_e and C_e). Population A_e rims also grew, but evidently could not accommodate as much growth as population A_n. Thus, the difference in A-population characteristics explains the presence of two additional populations in experiments, compared to one in the meteorite. If the volume fraction of population B_e is essentially that which would have grown on the rims of population A_e had there been more available outer surface area, the sum of the volume fractions of A_e and B_e (Φ_{A+B}) should be close to that of A_n ($\Phi = 0.50$). Indeed, $\Phi_{A+B} = 0.49$–0.50 for Y98*-f65 and Y98*-f68.

Cristobalite

The crystallization of cristobalite from a melt that has evolved only to a basaltic andesite composition is puzzling. In mafic rocks, if SiO_2 phases appear, they typically appear late in the crystallization sequence, as in basaltic shergottites Los Angeles (Rubin et al. 2000) and NWA 856 (Leroux and Cordier 2006), and olivine-phyric shergottite NWA 5789 (Gross et al. 2011). Liquid immiscibility is another cited mechanism for silica saturation in mafic materials (e.g., lunar basalt 70017; Rutherford et al. 1974). However, Y98*-f69ii is only 47 vol% crystalline, and petrographic evidence for liquid immiscibility is absent. The appearance of cristobalite around the entire outer surface of the bead suggests a favorable condition at the melt–gas interface, although crystals also appear elsewhere in the sample. Extreme volatile depletion at this interface would increase silica activity in the melt and expand the cristobalite stability field (Mathieu et al. 2011). Indeed, compared with other experimental runs, Y98*-f69 glass is considerably poorer in Na_2O (Fig. S18). However, for the given bulk composition (where Na is a minor element), Na_2O loss cannot increase SiO_2 activity enough to explain the presence of cristobalite (MELTS supplemental calculator; Ghiorso and Sack 1995). On a local scale, however, equilibrium thermodynamics cannot be assumed. Referencing a simple forsterite-silica binary phase diagram, if small areas of melt become enriched in silica, a local shift to the silica side of the eutectic could occur, resulting in cristobalite precipitation. The formation of this phase remains unclear, but it is likely attributable to local kinetic effects exacerbated by the abrupt hundredfold increase in cooling rate.

Inferences from P-enrichment Patterns in Natural Olivine

Phosphorus distribution in the natural phenocrysts provides tantalizing evidence for diffusion-controlled early olivine growth in Y-980459 (Fig. 5). As observed by Welsch et al. (2013), olivine crystals in magma reservoirs preserve a variety of morphologies indicating early diffusion-limited growth which may be overprinted by slower, interface-controlled growth; P-enrichment occurs at the highest growth rates (Milman-Barris et al. 2008; Welsch et al. 2014) and thus the presence of both P-rich and P-poor areas in externally faceted crystals preserves evidence of highly variable growth rate through time. The presence of P-rich lamellae in the Y-980459 olivine phenocrysts suggests that not all growth was slow, relative to the diffusivity of P in the melt. The skeletal shapes of experimental Y98* olivine crystals could represent an intermediate morphology experienced by Y-980459 olivine crystals between initial dendritic growth and final infilling (Welsch et al. 2014).

The preservation of melt inclusions near, but not within, phosphorus-rich zones is consistent with previous observations (Shearer et al. 2013) and the interpretation that they owe their existence to initially skeletal growth but were trapped during slow, near-equilibrium growth (Welsch et al. 2014). In their analysis of both transitional embayments and fully enclosed inclusions, Faure and Schiano (2005) demonstrate that the latter accurately preserve the far-field liquid composition at the time of entrapment precisely because slow growth is required to seal them off. However, this inference may not apply to the melt inclusions in Y-980459 olivine phenocrysts, because they are pervaded by cracks (Fig. 5).

Evaluation of Experiments According to Match Criteria

The relative success of experiments in reproducing features of Y-980459 can be evaluated according to the criteria outlined in the Introduction:

1. *Phase assemblage:* All experimental runs, with the exception of Y98*-f64 and one bead of Y98*-f69, produced the meteorite phase assemblage of olivine + Cr-spinel + pyroxene + glass. The presence of plagioclase in Y98*-f64 provides a lower limit on natural Stage 2 cooling at 50 °C h^{-1}.
2. *Modal proportions:* LT experimental products lacking plagioclase preserved significantly more glass than Y-980459, hinting that 28 °C h^{-1} is too fast for Stage 1 cooling. Among the LT runs, those with slower Stage 2 cooling are more crystalline,

suggesting that natural cooling rates were closer to 100 °C h^{-1} than 1000 °C h^{-1}. The HT series contains the samples with crystallinity most similar to the meteorite (Y98*-f65 and Y98*-f68). These experiments also have similar mineral modes to Y-980459.

3. *Phenocryst texture:* Quantitative analysis of pyroxene population A_e demonstrates that 10 °C h^{-1} is the best estimate for the Stage 1 cooling rate of population A_n. Although not a phenocryst phase, spinel morphology corroborates that 28 °C h^{-1} is too fast for Stage 1. The skeletal nature of experimental olivine phenocrysts, even during the slowest-cooled HT run, suggests a cooling rate <1°C h^{-1} for the final faceting of Y-980459 olivine phenocrysts. We refer to this stage of olivine phenocryst formation as Stage 0, since it is distinct from pyroxene phenocryst formation but was not constrained explicitly by experiments.
4. *Phase compositions:* Stage 2 cooling rates of 50 and 100 °C h^{-1} and Stage 1 cooling rates of 28 and 10 °C h^{-1} produced residual glass compositions closest to those of Y-980459.
5. *Groundmass crystal texture:* Quantitative analysis of pyroxene population C_e shows the best match to population C_n at cooling rates near 150 °C h^{-1}.

Although no single experiment exactly replicates all the characteristics of Y-980459, the run that is considered the best match to Y-980459 is Y98*-f65, cooled at Stage 1 = 10 °C h^{-1} and Stage 2 = 100 °C h^{-1}. In summary, experiments indicate that the initial cooling of Y-980459 must have been <1°C h^{-1}, followed by at least two subsequent cooling stages in which cooling rate increased from ~10 °C h^{-1} to ~100 °C h^{-1}.

Comparison to Previous Work

The cooling rate estimates derived here specifically for magma of Y-980459 composition can be used to evaluate estimates from previous studies. Olivine phenocryst cooling rates <1°C h^{-1} are in agreement with rates proposed by Miyamoto et al. (2009a) (0.2 °C h^{-1}) and with the slow end of ranges proposed by Greshake et al. (2004) (0.5–2 °C h^{-1}) and Mikouchi et al. (2004) (0.03–5 °C h^{-1}). Pyroxene phenocryst cooling around 10 °C h^{-1} is higher than the range proposed by Lentz and McSween 2005 (3–7 °C h^{-1}), but if the entire 5–16 °C h^{-1} range in Fig. 7A is considered, there is overlap. It is also probable that the cooling rate increase between Stage 0 and Stage 1 in nature was not as abrupt as that between Stage 1 and Stage 2. Thus, pyroxene phenocrysts may have experienced a range of increasing cooling rates (Greshake et al. 2004), with most crystallization occurring at cooling rates near 10°C h^{-1}. Finally, groundmass crystallization around 100 °C h^{-1} is more than 10 times slower than the 1450–1890 °C h^{-1} range proposed by Greshake et al. (2004).

Application to NWA 5789

Olivine-phyric shergottite NWA 5789 is similar to Y-980459 in bulk composition (Table 1), phenocryst morphology, and phase compositions (Gross et al. 2011). Because of these similarities, the results of the present study are broadly applicable to NWA 5789. The euhedral olivine megacrysts in NWA 5789 likely formed under conditions similar to those inferred for Y-980459, growing their final, faceted forms at cooling rates <1°C h^{-1}. The morphology of pyroxene phenocrysts in NWA 5789 is qualitatively similar to that of population A_n in Y-980459 (Gross et al. 2011), hinting that crystallization occurred during cooling at ~10 °C h^{-1}. A refined estimate would require quantification of S_v^P for the NWA 5789 crystal populations, as we present herein for Y-980459. One key difference from Y-980459 is the presence of a holocrystalline, plagioclase-bearing mesostasis in NWA 5789. Based on the experimental dataset developed in this study, cooling of the NWA 5789 mesostasis probably occurred at <50 °C h^{-1}. The presence of interstitial silica and merrillite (Gross et al. 2011), absent from Y-980459, also support slower cooling.

The putative crystallization history of NWA 5789 includes olivine megacryst and pyroxene core formation at up to 85 km depth, based partly on Al/Ti ratios in pyroxene (Gross et al. 2011). Later emplacement on or near the Martian surface is suggested to produce the mesostasis texture (Gross et al. 2011). This sequence is nearly identical to the overall volcanic history previously suggested for Y-980459 (e.g., Greshake et al. 2004; Usui et al. 2008), which we refine below with constraints provided by quantitative textural analysis in consultation with the experimental data set.

Cooling Model

We applied a numerical model of conductive lava flow cooling (Patrick et al. 2004) to Y-980459 crystallization in order to constrain the depths of crystallization using the derived cooling rates. Inputs specific to Mars or Y-980459 include lava density, Martian surface temperature, and crystal fraction (Table S6). The model was run with two sets of starting parameters, corresponding to Stage 1 and Stage 2. In both cases, we constrained the depth below the flow top where Y-980459 could have crystallized. In this set-up, the crystallizing portion of interest is unaffected by cooling from the bottom surface of the flow.

Model calculations suggest that crystallization depths are 25–45 cm for A_n pyroxenes (with a depth of 32 cm corresponding to a cooling rate of ~10 °C h^{-1}) and 5–7 cm for groundmass crystals. These are corroborated by direct observations of lava flow temperatures at Kīlauea volcano. Thermocouple measurements from 20 cm deep in an actively inflating pāhoehoe flow indicate cooling rates around 20 °C h^{-1} over the crystallization interval (calculated from data in Hon et al. 1994); at 6 cm deep, cooling is around 85 °C h^{-1}. Thus, model depth estimates appear reasonable in light of relevant field data.

Remotely observed terrestrial pāhoehoe flows exhibit surface cooling rates of thousands of °C h^{-1} (e.g., Ball et al. 2008) to ≤900 °C h^{-1} (Flynn and Mouginis-Mark 1992). Modeled cooling rates agree with the higher end of these measurements, yet predict cooling rates >1450°C h^{-1} only within the upper 2 cm of the flow. This depth interval is smaller than the smallest length dimension of the Y-980459 meteorite (Misawa 2004). Therefore, the entirety of Y-980459 could not have cooled at rates >1450 °C h^{-1}. This model-based inference supports the experimental conclusion that groundmass crystallization was on the order of 100 °C h^{-1}, rather than 1000 °C h^{-1}.

IMPLICATIONS

Volcanological Context

The igneous history of Y-980459 may be quite similar to that of a primitive terrestrial basalt. Melt inclusion CO_2 contents suggest that olivine phenocryst growth took place at ~30 km depth (Usui et al. 2012). Pyroxene phenocrysts may have begun crystallizing at depth, as suggested by Greshake et al. (2004) and consistent with geochemical evidence (Fig. 9), but the cooling rates derived in this study (5–16 °C h^{-1}) imply that population A_n crystallized mainly in a surficial environment. Insulated lava tube systems cool too slowly (<1 °C h^{-1} using reasonable velocities; Ho and Cashman 1997; Thordarson and Self 1998), whereas lava in open channels cools too quickly (22–50 °C h^{-1}; Cashman et al. 1999). Rather, A_n crystals may have formed predominantly in an environment analogous to a pāhoehoe flow (Fig. 11). For example, an inflating lobe on the order of decimeters thick may have crystallized population A_n. A subsequent break-out could produce cooling rates necessary for population C_n and olivine dendrites to form and then quench the residual melt.

A three-stage cooling model for Y-980459 was proposed by Usui et al. (2008). The recognized need for separate stages of olivine, pyroxene, and groundmass crystallization is in agreement with our findings. However, the suggestion that pyroxene phenocrysts formed dominantly before eruption is not consistent with cooling rates derived in this study. It has been previously suggested that Y-980459 represents a parcel of lava that cooled in a tumulus and later broke out (Lentz and McSween 2005). Our results agree with this scenario, while not specifically requiring a tumulus structure.

Breakouts from the interiors of ‘a‘ā flows may manifest as pāhoehoe (Jurado-Chichay and Rowland 1995). It is also possible that population A_n crystallized in the upper few cm of a single thick flow. However, the presence of a pāhoehoe flow field composed of layered cooling units (Walker 1971) provides a vastly greater proportion of material matching the thermal history of Y-980459 compared with the single cooling unit scenario (Fig. 11). Thus, Y-980459 may represent a relatively common terrestrial lava emplacement mechanism. Our interpretation of crystallization history (Fig. 11) is consistent with previous work on Y-980459 (Greshake et al. 2004; Usui et al. 2008, 2012) and resolves likely lava flow emplacement conditions in greater detail. A similar volcanological history is broadly consistent with proposed thermal paths experienced by other olivine-phyric shergottites, including NWA 1068 (Barrat et al. 2002a, 2002b; Filiberto et al. 2010), LAR 06319 (Filiberto et al. 2010; Balta et al. 2013), and NWA 5789 (Gross et al. 2011). To the extent that Y-980459 is a representative sample of its source area on the surface of Mars, our inference that it represents a pāhoehoe flow field connotes general relevance of this lava emplacement mechanism for the basaltic and olivine-phyric shergottite lavas.

Emplacement on Mars: A Typical Sample of a Typical Flow?

Most features of terrestrial effusive basaltic volcanism have been identified on Mars, including stacked flows, flood lavas, thin (<1 m) flow margins, and inflated sheet flows (Keszthelyi et al. 2008). Of particular interest to the study of Y-980459 are the flood lavas, or long lava flows (e.g., Cashman et al. 1998; Keszthelyi et al. 2004), analogous to terrestrial flood basalts. Although these terrestrial counterparts were originally interpreted to require high effusion rates (Shaw and Swanson 1970), more recent works (see summary by Cashman et al. 1998) recognize inflation features and suggest that many flood basalts were emplaced at lower effusion rates (e.g., ~10–10^3 m^3 s^{-1}; Keszthelyi and Self 1998). There is growing evidence that some flood basalts are composed of compound, inflated pāhoehoe flows (Hon et al. 1994; Self et al.

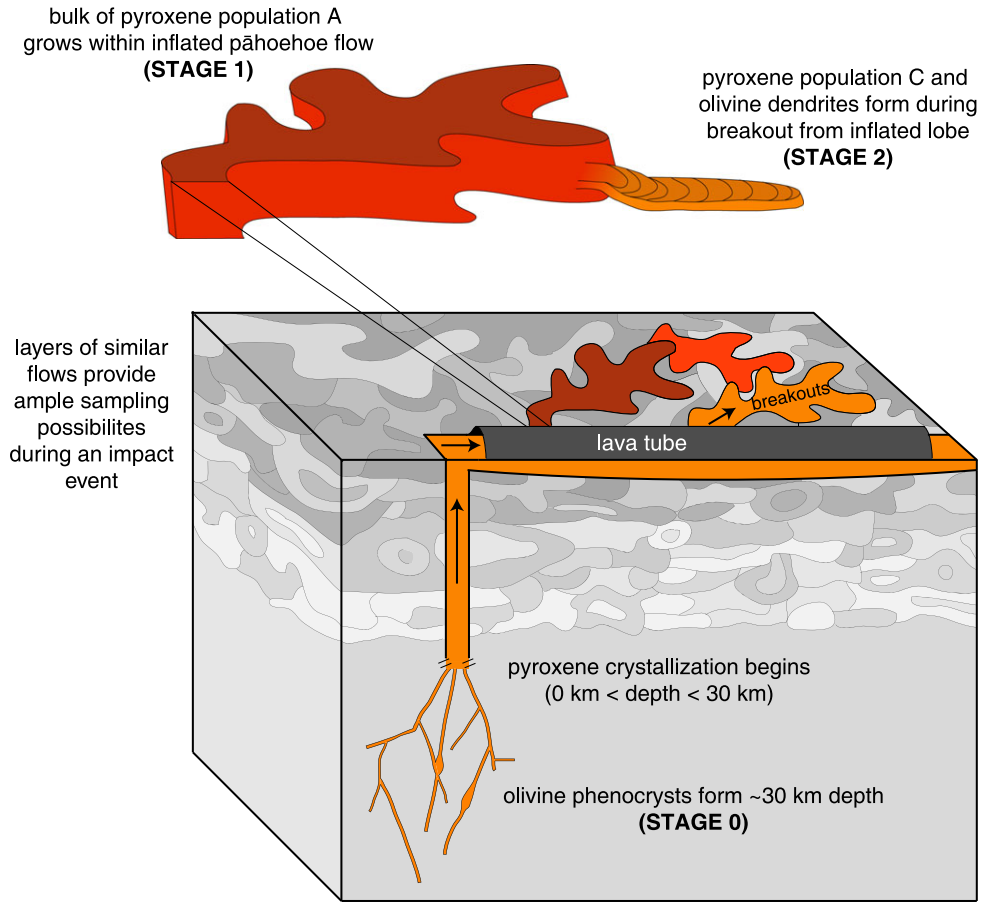

Fig. 11. Schematic representation of the igneous cooling history of Y-980459, emphasizing the repetitive nature of a field of pāhoehoe-like flows. Estimate of ~30 km depth from Usui et al. (2012).

1996; Vye-Brown et al. 2013). This particular emplacement mechanism encompasses cooling rates that could be relevant to Y-980459, from thicker, more insulated lobes to thin breakouts at the flow margin.

Flood lavas in the Cerberus plains illustrate the occurrence of such systems on Mars. The flows are >1500 km long, exhibiting both inflated margins and "platy-ridged" morphology similar to those of the Laki Flow Field in Iceland (Keszthelyi et al. 2004). This terrestrial analogy suggests that the Martian structures can be formed by pāhoehoe-like sheet flows, consistent with modeling that indicates a high thermal efficiency for platy-ridged flows (Keszthelyi et al. 2004). These pāhoehoe-like long flows may be thick overall, although individual lobes can be thin, in keeping with possible emplacement mechanisms for Y-980459.

In this sense (pāhoehoe lobe), model depths are in accord with previous inferences of a thin lava flow as the source of Y-980459. However, the flow field may be composed of many individual lobes stacked atop one another, resulting in a flow that is actually quite thick. Thus, we make the distinction between an anomalously thin flow and a fairly typical basaltic lava flow with thin individual cooling units. This type of flow is widespread on Earth (Self et al. 1998) and has been observed in remote sensing imagery from Mars (Keszthelyi et al. 2008; Hauber et al. 2009), making it a viable mechanism for the emplacement of Y-980459 and conceivably other shergottites.

Acknowledgments—This work was supported by NASA Mars Fundamental Research grant NNX11AM29G (JH). ECF was partially supported by the Fred M. Bullard Graduate Fellowship and an ARCS Honolulu award during this project. The National Institute of Polar Research (Tokyo) provided the thin section of Y-980459. We thank Eric Hellebrand for assistance in collecting and analyzing microprobe data, Patrick Gasda for Raman data, Tanis Leonhardi for electroplating work, and Matt Patrick for sharing his MATLAB code. We appreciate comments from Jeff Taylor, Mike Garcia, and Benoît Welsch on an earlier

version of this manuscript and discussions on Martian volcanism with Scott Rowland. Reviews by Malcolm Rutherford, Steve Elardo, and an anonymous reviewer improved the final paper. We thank Kevin Righter for thoughtful editorial handling. This is SOEST publication #9586.

Editorial Handling—Dr. Kevin Righter

REFERENCES

Albarede F. and Bottinga Y. 1972. Kinetic disequilibrium in trace element partitioning between phenocrysts and host lava. *Geochimica et Cosmochimica Acta* 36:141–156.

Armstrong J. T. 1988. Quantitative analysis of silicate and oxide materials: Comparison of Monte Carlo, ZAF, and ϕ (ρz) procedures. Proceedings, 23rd Annual Conference of the Microbeam Analysis Society. pp. 239–246.

Ball M., Pinkerton H., and Harris A. J. L. 2008. Surface cooling, advection and the development of different surface textures on active lavas on Kilauea, Hawai'i. *Journal of Volcanology and Geothermal Research* 173:148–156.

Balta J. B., Sanborn M., McSween H. Y., and Wadhwa M. 2013. Magmatic history and parental melt composition of olivine-phyric shergottite LAR 06319: Importance of magmatic degassing and olivine antecrysts in Martian magmatism. *Meteoritics & Planetary Science* 48:1359–1382.

Balta J. B., Sanborn M. E., Udry A., Wadhwa M., and McSween H. Y. 2015. Petrology and trace element geochemistry of Tissint, the newest shergottite fall. *Meteoritics & Planetary Science* 50:63–85.

Barrat J. A., Gillet P., Sautter V., Jambon A., Javoy M., Göpel C., Lesourd M., Keller F., and Petit E. 2002a. Petrology and chemistry of the basaltic shergottite North West Africa 480. *Meteoritics & Planetary Science* 37:487–499.

Barrat J. A., Jambon A., Bohn M., Gillet P., Sautter V., Göpel C., Lesourd M., and Keller F. 2002b. Petrology and chemistry of the picritic shergottite Northwest Africa 1068 (NWA 1068). *Geochimica et Cosmochimica Acta* 66:3505–3518.

Blinova A. and Herd C. D. K. 2009. Experimental study of polybaric REE partitioning between olivine, pyroxene and melt of the Yamato 980459 composition: Insights into the petrogenesis of depleted shergottites. *Geochimica et Cosmochimica Acta* 73:3471–3492.

Brachfeld S., Shah D., First E., Hammer J., and Bowles J. 2015. Influence of redox conditions on the intensity of Mars crustal magnetic anomalies. *Meteoritics & Planetary Science* 50:1703–1717. doi:10.1111/maps.12505.

Bryan W. B. 1972. Morphology of quench crystals in submarine basalts. *Journal of Geophysical Research* 77:5812–5819.

Cashman K., Pinkerton H., and Stephenson J. 1998. Introduction to special section: Long lava flows. *Journal of Geophysical Research: Solid Earth* 103:27,281–27,289.

Cashman K. V., Thornber C., and Kauahikaua J. P. 1999. Cooling and crystallization of lava in open channels, and the transition of pāhoehoe lava to 'a'ā. *Bulletin of Volcanology* 61:306–323.

Donaldson C. H. 1976. An experimental investigation of olivine morphology. *Contributions to Mineralogy and Petrology* 57:187–213.

Donaldson C. H., Williams R. J., and Lofgren G. 1975. A sample holding technique for study of crystal growth in silicate melts. *American Mineralogist* 60:324–326.

Donovan J. J. and Tingle T. N. 1996. An improved mean atomic number background correction for quantitative microanalysis. *Microscopy and Microanalysis* 2:1–7.

Dowty E. 1980. Crystal growth and nucleation theory and the numerical simulation of igneous crystallization. In *Physics of magmatic processes*, edited by Hargraves R. B. Princeton, New Jersey: Princeton University Press. pp. 419–486.

Edgar A. D. 1973. *Experimental petrology: Basic principles and techniques*. Oxford: Clarendon Press. p. 240.

Faure F. and Schiano P. 2005. Experimental investigation of equilibrium conditions during forsterite growth and melt inclusion formation. *Earth and Planetary Science Letters* 236:882–898.

Faure F., Trolliard G., Nicollet C., and Montel J.-M. 2003. A developmental model of olivine morphology as a function of the cooling rate and the degree of undercooling. *Contributions to Mineralogy and Petrology* 145:251–263.

Faure F., Schiano P., Trolliard G., Nicollet C., and Soulestin B. 2007. Textural evolution of polyhedral olivine experiencing rapid cooling rates. *Contributions to Mineralogy and Petrology* 153:405–416.

Filiberto J. and Dasgupta R. 2011. Fe^{2+}–Mg partitioning between olivine and basaltic melts: Applications to genesis of olivine-phyric shergottites and conditions of melting in the Martian interior. *Earth and Planetary Science Letters* 304:527–537.

Filiberto J., Musselwhite D. S., Gross J., Burgess K., Le L., and Treiman A. H. 2010. Experimental petrology, crystallization history, and parental magma characteristics of olivine-phyric shergottite NWA 1068: Implications for the petrogenesis of "enriched" olivine-phyric shergottites. *Meteoritics & Planetary Science* 45:1258–1270.

Flynn L. P. and Mouginis-Mark P. J. 1992. Cooling rate of an active Hawaiian lava flow from nighttime spectroradiometer measurements. *Geophysical Research Letters* 19:1783–1786.

Ghiorso M. S. and Sack R. O. 1995. Chemical mass transfer in magmatic processes IV. A revised and internally consistent thermodynamic model for the interpolation and extrapolation of liquid-solid equilibria in magmatic systems at elevated temperatures and pressures. *Contributions to Mineralogy and Petrology* 119:197–212.

Greshake A., Fritz J., and Stöffler D. 2004. Petrology and shock metamorphism of the olivine-phyric shergottite Yamato 980459. *Geochimica et Cosmochimica Acta* 68:2359–2377.

Gross J., Treiman A. H., Filiberto J., and Herd C. D. K. 2011. Primitive olivine-phyric shergottite NWA 5789: Petrography, mineral chemistry, and cooling history imply a magma similar to Yamato 980459. *Meteoritics & Planetary Science* 46:116–133.

Grove T. L. 1981. Use of FePt alloys to eliminate the iron loss problem in 1 atmosphere gas mixing experiments: Theoretical and practical considerations. *Contributions to Mineralogy and Petrology* 78:298–304.

Hammer J. E. 2006. Influence of fO_2 and cooling rate on the kinetics and energetics of Fe-rich basalt crystallization. *Earth and Planetary Science Letters* 248:618–637.

Hammer J. E. 2009. Application of a textural geospeedometer to the late-stage magmatic history of MIL 03346. *Meteoritics & Planetary Science* 44:141–154.

Hauber E., Bleacher J., Gwinner K., Williams D., and Greeley R. 2009. The topography and morphology of low shields and associated landforms of plains volcanism in the Tharsis region of Mars. *Journal of Volcanology and Geothermal Research* 185:69–95.

Hilliard J. E. 1968. Measurement of volume in volume. In *Quantitative microscopy*, edited by DeHoff R. T. and Rhines F. N. New York: McGraw-Hill. pp. 45–76.

Ho A. M. and Cashman K. V. 1997. Temperature constraints on the Ginkgo flow of the Columbia River Basalt Group. *Geology* 25:403–406.

Hon K., Kauahikaua J., Denlinger R., and Mackay K. 1994. Emplacement and inflation of pahoehoe sheet flows: Observations and measurements of active lava flows on Kilauea Volcano, Hawaii. *Geological Society of America Bulletin* 106:351–370.

Hon K., Gansecki C., and Kauahikaua J. 2003. The transition from ʻaʻā to pāhoehoe crust on flows emplaced during the Pu'u ʻŌʻō-Kūpaianaha eruption. *USGS Professional Paper* 1676:89–104.

Hort M., Marsh B. D., Resmini R. G., and Smith M. K. 1999. Convection and crystallization in a liquid cooled from above: An experimental and theoretical study. *Journal of Petrology* 40:1271–1300.

Ikeda Y. 2004. Petrology of the Yamato 980459 shergottite. *Antarctic Meteorite Research* 17:35–54.

Irving A. J., Kuehner S. M., Herd C. D. K., Gellissen M., Korotev R. L., Puchtel I., Walker R. J., Lapen T. J., and Rumble D. III 2010. Petrologic, elemental and multi-isotopic characterization of permafic olivine-phyric shergottite Northwest Africa 5789: A primitive magma derived from depleted Martian mantle (abstract #1547). 41st Lunar and Planetary Science Conference. CD-ROM.

Jarosewich E., Nelen J. A., and Norberg J. A. 1980. Reference samples for electron microprobe analysis. *Geostandards Newsletter IV* 4:3–47.

Jurado-Chichay Z. and Rowland S. K. 1995. Channel overflows of the Pōhue Bay flow, Mauna Loa, Hawaiʻi: Examples of the contrast between surface and interior lava. *Bulletin of Volcanology* 57:117–126.

Kessel R., Beckett J. R., and Stolper E. M. 2001. Thermodynamic properties of the Pt-Fe system. *American Mineralogist* 86:1003–1014.

Keszthelyi L. and Self S. 1998. Some physical requirements for the emplacement of long basaltic lava flows. *Journal of Geophysical Research: Solid Earth* 103:27,447–27,464.

Keszthelyi L., Thordarson T., McEwen A., Haack H., Guilbaud M.-N., Self S., and Rossi M. J. 2004. Icelandic analogs to Martian flood lavas. *Geochemistry, Geophysics, Geosystems* 5:Q11014. doi:10.1029/2004GC000758.

Keszthelyi L., Jaeger W., McEwen A., Tornabene L., Beyer R. A., Dundas C., and Milazzo M. 2008. High Resolution Imaging Science Experiment (HiRISE) images of volcanic terrains from the first 6 months of the Mars Reconnaissance Orbiter Primary Science Phase. *Journal of Geophysical Research* 113:E04005. doi:10.1029/2007JE002968.

Kirkpatrick R. J. 1981. Kinetics of crystallization in igneous rocks. In *Kinetics of geochemical processes*, edited by Lasaga A. C. and Kirkpatrick R. J. Chantilly, Virginia: Mineralogical Society of America. pp. 321–398.

Kouchi A., Tsuchiyama A., and Sunagawa I. 1986. Effect of stirring on crystallization kinetics of basalt: Texture and element partitioning. *Contributions to Mineralogy and Petrology* 93:429–438.

Lasaga A. C. 1982. Toward a master equation in crystal growth. *American Journal of Science* 282:1264–1288.

Lentz R. C. F. and McSween H. Y. Jr. 2005. A textural examination of the Yamato 980459 and Los Angeles shergottites using crystal size distribution analysis. *Antarctic Meteorite Research* 18:66–82.

Leroux H. and Cordier P. 2006. Magmatic cristobalite and quartz in the NWA 856 Martian meteorite. *Meteoritics & Planetary Science* 41:913–923.

Lessel J. and Putirka K. 2015. New thermobarometers for Martian igneous rocks, and some implications for secular cooling on Mars. *American Mineralogist* 100:2163–2171. doi:10.2138/am-2015-4732.

Lloyd A. S., Plank T., Ruprecht P., Hauri E. H., and Rose W. 2013. Volatile loss from melt inclusions in pyroclasts of differing sizes. *Contributions to Mineralogy and Petrology* 165:129–153.

Lofgren G. 1980. Experimental studies on the dynamic crystallization of silicate melts. In *Physics of magmatic processes*, edited by Hargraves R. B. Princeton, New Jersey: Princeton University Press. pp. 487–551.

Lofgren G., Williams R. J., Usselman T. M., Donaldson C. H., and Mullins O. Jr. 1974. Experimentally reproduced textures and mineral chemistry of Apollo 15 quartz normative basalts. Proceedings, 5th Lunar Science Conference. pp. 549–567.

Macdonald G. A. 1953. Pahoehoe, aa, and block lava. *American Journal of Science* 251:169–191.

Mathieu R., Libourel G., Deloule E., Tissandier L., Rapin C., and Podor R. 2011. Na_2O solubility in CaO–MgO–SiO_2 melts. *Geochimica et Cosmochimica Acta* 75:608–628.

McCanta M. C., Beckett J. R., and Stolper E. M. 2016. Correlations and zoning patterns of phosphorus and chromium in olivine from H chondrites and the LL chondrite Semarkona. *Meteoritics & Planetary Science*. doi:10.1111/maps.12604.

McCoy T. J. and Lofgren G. E. 1999. Crystallization of the Zagami shergottite: An experimental study. *Earth and Planetary Science Letters* 173:397–411.

McCoy T., Taylor G., and Keil K. 1992. Zagami: Product of a 2-stage magmatic history. *Geochimica et Cosmochimica Acta* 56:3571–3582.

Mikouchi T., Miyamoto M., and McKay G. A. 1998. Mineralogy of Antarctic basaltic shergottite Queen Alexandra Range 94201: Similarities to Elephant Moraine A79001 (lithology B) Martian meteorite. *Meteoritics & Planetary Science* 33:181–189.

Mikouchi T., Koizumi E., McKay G., Monkawa A., Ueda Y., Chokai J., and Miyamoto M. 2004. Yamato 980459: Mineralogy and petrology of a new shergottite-related rock from Antarctica. *Antarctic Meteorite Research* 17:13–34.

Milman-Barris M. S., Beckett J. R., Baker M. B., Hofmann A. E., Morgan Z., Crowley M. R., Vielzeuf D., and Stolper E. 2008. Zoning of phosphorus in igneous olivine. *Contributions to Mineralogy and Petrology* 155:739–765.

Misawa K. 2003. The Yamato 980459 shergottite consortium (abstract). International symposium: Evolution of solar system materials. pp. 84–85.

Misawa K. 2004. The Yamato 980459 olivine-phyric shergottite consortium. *Antarctic Meteorite Research* 17:1–12.

Miyamoto M., McKay D. S., McKay G. A., and Duke M. B. 1986. Chemical zoning and homogenization of olivines in ordinary chondrites and implications for thermal histories of chondrules. *Journal of Geophysical Research: Solid Earth* 91:12,804–12,816.

Miyamoto M., Koizumi E., and Mikouchi T. 2009a. Cooling rates of Y980459 and DaG 476 shergottites on the basis of Fe-Mg zoning of olivine (abstract #1143). 40th Lunar and Planetary Science Conference. CD-ROM.

Miyamoto M., Mikouchi T., and Jones R. H. 2009b. Cooling rates of porphyritic olivine chondrules in the Semarkona (LL3. 00) ordinary chondrite: A model for diffusional equilibration of olivine during fractional crystallization. *Meteoritics & Planetary Science* 44:521–530.

Mollo S., Del Gaudio P., Ventura G., Iezzi G., and Scarlato P. 2010. Dependence of clinopyroxene composition on cooling rate in basaltic magmas: Implications for thermobarometry. *Lithos* 118:302–312.

Musselwhite D. S., Dalton H. A., Kiefer W. S., and Treiman A. H. 2006. Experimental petrology of the basaltic shergottite Yamato 980459: Implications for the thermal structure of the Martian mantle. *Meteoritics & Planetary Science* 41:1271–1290.

Nekvasil H., Dondolini A., Horn J., Filiberto J., Long H., and Lindsley D. H. 2004. The origin and evolution of silica-saturated alkalic suites: An experimental study. *Journal of Petrology* 45:693–721.

O'Neill H. S. C., Pownceby M. I., and McCammon C. A. 2003. The magnesiowüstite: Iron equilibrium and its implications for the activity-composition relations of (Mg, Fe)2SiO4 olivine solid solutions. *Contributions to Mineralogy and Petrology* 146:308–325.

Patrick M. R., Dehn J., and Dean K. 2004. Numerical modeling of lava flow cooling applied to the 1997 Okmok eruption: Approach and analysis. *Journal of Geophysical Research* 109:B03202. doi:10.1029/2003JB002537.

Presnall D. C. and Brenner N. L. 1974. A method for studying iron silicate liquids under reducing conditions with negligible iron loss. *Geochimica et Cosmochimica Acta* 38:1785–1788.

Putirka K., Johnson M., Kinzler R., Longhi J., and Walker D. 1996. Thermobarometry of mafic igneous rocks based on clinopyroxene-liquid equilibria, 0–30 kbar. *Contributions to Mineralogy and Petrology* 123:92–108.

Rubin A. E., Warren P. H., Greenwood J. P., Verish R. S., Leshin L. A., Hervig R. L., Clayton R. N., and Mayeda T. K. 2000. Los Angeles: The most differentiated basaltic Martian meteorite. *Geology* 28:1011–1014.

Rutherford M. J., Hess P. C., and Daniel G. H. 1974. Experimental liquid line of descent and liquid immiscibility for basalt 70017. Proceedings, 5th Lunar Science Conference. pp. 569–583.

Schneider C. A., Rasband W. S., and Eliceiri K. W. 2012. NIH Image to ImageJ: 25 years of image analysis. *Nature Methods* 9:671–675.

Self S., Thordarson T., Keszthelyi L., Walker G. P. L., Hon K., Murphy M. T., Long P., and Finnemore S. 1996. A new model for the emplacement of Columbia River basalts as large, inflated pahoehoe lava flow fields. *Geophysical Research Letters* 23:2689–2692.

Self S., Keszthelyi L., and Thordarson T. 1998. The importance of pāhoehoe. *Annual Review of Earth and Planetary Sciences* 26:81–110.

Shaw H. R. and Swanson D. A. 1970. Eruption and flow rates of flood basalts. Proceedings, Second Columbia River Basalt Symposium. pp. 271–299.

Shearer C. K., McKay G., Papike J. J., and Karner J. M. 2006. Valence state partitioning of vanadium between olivine-liquid: Estimates of the oxygen fugacity of Y980459 and application to other olivine-phyric Martian basalts. *American Mineralogist* 91:1657–1663.

Shearer C. K., Aaron P. M., Burger P. V., Guan Y., Bell A. S., and Papike J. J. 2013. Petrogenetic linkages among fO_2, isotopic enrichments-depletions and crystallization history in Martian basalts. Evidence from the distribution of phosphorus in olivine megacrysts. *Geochimica et Cosmochimica Acta* 120:17–38.

Thordarson T. and Self S. 1998. The Roza Member, Columbia River Basalt Group: A gigantic pahoehoe lava flow field formed by endogenous processes? *Journal of Geophysical Research-Solid Earth* 103:27,411–27,445.

Treiman A. and Sutton S. 1992. Petrogenesis of the Zagami meteorite: Inferences from synchrotron X-ray (SXRF) microprobe and electron microprobe analyses of pyroxenes. *Geochimica et Cosmochimica Acta* 56:4059–4074.

Underwood E. E. 1968. Surface area and length in volume. In *Quantitative microscopy*, edited by DeHoff R. T. and Rhines F. N. New York: McGraw-Hill. pp. 77–127.

Usui T., McSween H. Y., and Floss C. 2008. Petrogenesis of olivine-phyric shergottite Yamato 980459, revisited. *Geochimica et Cosmochimica Acta* 72:1711–1730.

Usui T., Alexander C. M. O'D, Wang J., Simon J. I., and Jones J. H. 2012. Origin of water and mantle–crust interactions on Mars inferred from hydrogen isotopes and volatile element abundances of olivine-hosted melt inclusions of primitive shergottites. *Earth and Planetary Science Letters* 357–358:119–129.

Vona A. and Romano C. 2013. The effects of undercooling and deformation rates on the crystallization kinetics of Stromboli and Etna basalts. *Contributions to Mineralogy and Petrology* 166:491–509.

Vye-Brown C., Self S., and Barry T. L. 2013. Architecture and emplacement of flood basalt flow fields: Case studies from the Columbia River Basalt Group, NW USA. *Bulletin of Volcanology* 75:3. doi:10.1007/s00445-013-0697-2.

Walker G. P. L. 1971. Compound and simple lava flows and flood basalts. *Bulletin Volcanologique* 35:579–590.

Walker D., Powell M. A., Hays J. F., and Lofgren G. E. 1978. Dynamic crystallization of a eucrite basalt. Proceedings, 9th Lunar and Planetary Science Conference. pp. 1369–1391.

Welsch B., Faure F., Famin V., Baronnet A., and Bachelery P. 2013. Dendritic crystallization: A single process for all the textures of olivine in basalts? *Journal of Petrology* 54:539–574.

Welsch B., Hammer J., and Hellebrand E. 2014. Phosphorus zoning reveals dendritic architecture of olivine. *Geology* 42:867–870.

Wright T. L. and Okamura R. T. 1977. Cooling and crystallization of tholeiitic basalt, 1965 Makaopuhi Lava Lake, Hawaii. USGS Professional Paper 1004.

SUPPORTING INFORMATION

Additional supporting information may be found in the online version of this article:

Fig S1: Electroplating configuration. Current reading in the image shown (3.07 mA) is lower than the optimum values determined through trial and error (45–50 mA).

Fig S2: DelTech 1-atm gas mixing furnace at the University of Hawaii, Mānoa.

Fig S3: Evidence for P enrichment in Y98*-f18 (6 h at 1198.5 °C, followed by 3 h at 1434 °C, followed by cooling at 72 °C h^{-1} down to 1000 °C). At left, BSE image overlain with semi-transparent pink highlighting, showing areas of P enrichment seen in P X-ray map at right (lighter blue = higher concentration of P). Scale bar in BSE image is approximately 50 μm and applies to P-map as well. ol = olivine, px = pyroxene, gl = glass.

Fig S4: Bottom end of removable sample apparatus, shown after third quench wire was added.

Fig S5: Close-up of quench flask during a high-temperature run.

Fig S6: Backscattered electron (BSE) comparison of experimental run products on pure Pt wire and FePt wire. Both beads were held for 12 h at 1385 °C, cooled to 1113 °C at 28 °C h^{-1}, cooled to 909 °C at 320.6 °C h^{-1}, and quenched. Scale bar applies to A and B. A) Sample Y98*-f35(1) on Pt wire. Offsets in the mosaic are due to slight distortion that prevented perfect image alignment. B) Sample Y98*-f47i on FePt wire.

Fig S7: BSE images of isothermal experiments bracketing the plagioclase-in temperature (A) Y98*-f60i: held for 12 h at 1432 °C, cooled to 1133 °C at 300 °C h^{-1}, held for 26.47 h, and quenched. No plagioclase crystallized. (B) Y98*-f61: began with second bead of Y98*-f60, still intact and on wire, held at 1120 °C for 26.43 h and quenched. Plagioclase crystallized.

Fig S8: A) BSE images of Y98*-f55ii, superheated at 1548 °C for 16 h, cooled to 1391.5 °C at 1000 °C h^{-1}, held at 1391.5 °C for 12 h, cooled to 1116 °C at 28 °C h^{-1}, cooled to 909 °C at 320.6 °C h^{-1}, quenched. Black regions are likely glass, either unpolished or plucked during polishing. B) Reflected light images of run Y98*-f37, superheated at 1495 °C for 4 h, cooled to 1000 °C at 72 °C h^{-1}, quenched. Despite their vastly different cooling histories, the samples are very similar, suggesting that crystallization was dominantly controlled by the superheating step(s). In each sample, most of the charge is taken up by one or a few branching crystals of pyroxene, with glass and anhedral Cr-spinel grains filling the interstices.

Fig S9: BSE comparison of runs identical other than high temperature dwell time. Time temperature paths were 12/24 h dwell at 1432 °C, cooled to 909 °C at 320.6 °C h^{-1}, quenched. Scale bars are 200 μm. A) Y98*-f58ii, 12 h dwell. B) Y98*-f59ii, 24 h dwell.

Fig S10: BSE images of runs with a single, linear cooling rate. A) Y98*-f26a, held for 6 h at 1126.5 °C and 6 h at 1433.5 °C, then cooled to 1000 °C at 36 °C h^{-1}, quenched. Plagioclase is present. B) Y98*-f18, held for 6 h at 1198.5 °C and 3 h at 1434 °C, then cooled to 1000 °C at 72 °C h^{-1}, quenched. C) Y98*-f58ii, held 12 h at 1432 °C, then cooled to 909 °C at 320.6 °C h^{-1}, quenched.

Fig S11: BSE images of runs (A) Y98*-f50i, quenched at 859 °C and (B) Y98*-f48iii, quenched at 909 °C. Time-temperature paths were both as follows: 12 h at 1384.5 °C, cooled to 1113 °C at 28 °C h^{-1}, cooled to 859/909 °C at 320.6 °C h^{-1}, quenched. Scale bars are 500 μm.

Fig S12: BSE mosaic images of LT and HT experimental run products.

Fig S13: The two beads from the LT and HT series runs that contain many small crystals of olivine, accumulated at the base of the charge, instead of several large ones. Scale bars are 500 μm. A) Y98*-f57 (bead ii). B) Y98*-f63 (bead ii).

Fig S14: Example of pyroxene populations for one experimental bead (run Y98*-f65, see Table 2 in main text). Background is a BSE mosaic at 100× magnification. Blue highlights population Ae, pink highlights population Be, and green outlines areas containing population Ce.

Fig S15: BSE mosaic images of cooling experiments quenched at the end of Stage 1. No pyroxene crystals of populations Be or Ce are present. Scale bars are 500 μm. A)Y98*-f51, held 12 h at 1385 °C, cooled to 1113 °C at 28 °C h^{-1}, quenched. B)Y98*-f65-1, held 12 h at 1433 °C, cooled to 1115.5 °C at 10 °C h^{-1}, quenched. C)Y98*-f66-1ii, held 12 h at 1433 °C, cooled to 1116.5 °C at 1 °C h^{-1}, quenched.

Fig S16: BSE image of experiment Y98*-f69 (bead ii). Black, cross-shaped crystals with interior fracture patterns are cristobalite.

Fig S17: Composition of pyroxene crystals in experiments and Y-980459. Horizontal axis and legend apply to all three plots. No compositional trend with cooling rate is evident.

Fig S18: Glass compositions in Y-980459 and experiments. Error bars are shown in the upper left of each plot, when larger than the symbol size. Horizontal

axis and legend apply to all three plots. Open symbols indicate "intercumulus" glass; f69 points with black outlines indicate analyses from the cristobalite-bearing bead. Note the low TiO_2 content of the meteorite in (A), the Na_2O depletion of experiments in (B), and the heterogeneous nature of K_2O in (C).

Fig S19: Olivine compositions in experiments and Y-980459. Legend applies to both plots. Note the absence of cooling-rate dependent compositional trends. The high FeO, MnO points correspond to the low MgO, SiO_2 points.

Fig S20: Boundary layers preserved in the quenched glass of experiment Y98*-f67 and more subtly in Y-980459 (inset). Crystals in both images are pyroxene.

Table S1: Complete run table of all experiments mentioned in the article.

Table S2: Microprobe glass analyses, including standards.

Table S3: Microprobe olivine analyses, including standards.

Table S4: Microprobe pyroxene analyses, including standards.

Table S5: Complete surface area per unit volume data.

Table S6: Inputs to the conductive cooling model.